

# Compressional behavior and spin state of -(Al,Fe)OOH at high pressures

著者	Itaru Ohira, Jennifer M Jackson, Natalia V Solomatova, Wolfgang Sturhahn, Gregory J Finkelstein, Seiji Kamada, Takaaki Kawazoe, Fumiya Maeda, Naohisa Hirao, Satoshi Nakano, Thomas S Toellner, Akio Suzuki, Eiji Ohtani
journal or publication title	American Mineralogist
volume	104
number	9
page range	1273-1284
year	2019-09-03
URL	<a href="http://hdl.handle.net/10097/00129828">http://hdl.handle.net/10097/00129828</a>

doi: 10.2138/am-2019-6913

**Compressional behavior and spin state of  $\delta$ -(Al,Fe) OOH at high pressures**

**Itaru Ohira<sup>1,a\*</sup>, Jennifer M. Jackson<sup>2</sup>, Natalia V. Solomatova<sup>2,b</sup>, Wolfgang Sturhahn<sup>2</sup>, Gregory J. Finkelstein<sup>2,c</sup>, Seiji Kamada<sup>1,3</sup>, Takaaki Kawazoe<sup>4,5</sup>, Fumiya Maeda<sup>1</sup>, Naohisa Hirao<sup>6</sup>, Satoshi Nakano<sup>7</sup>, Thomas S. Toellner<sup>8</sup>, Akio Suzuki<sup>1</sup>, Eiji Ohtani<sup>1</sup>**

<sup>1</sup> Department of Earth Science, Graduate School of Science, Tohoku University, Sendai 980-8578, Japan

<sup>2</sup> Seismological Laboratory, California Institute of Technology, Pasadena, California 91125, U.S.A.

<sup>3</sup> Frontier Research Institute for Interdisciplinary Sciences, Tohoku University, Sendai 980-8578, Japan

<sup>4</sup> Bayerisches Geoinstitut, University of Bayreuth, Bayreuth, 95440 Germany

<sup>5</sup> Department of Earth and Planetary Systems Science, Graduate School of Science, Hiroshima University, Higashi-Hiroshima 739-8526, Japan

<sup>6</sup> Japan Synchrotron Radiation Research Institute (JASRI), Hyogo, 679-5198, Japan

<sup>7</sup> National Institute for Materials Science (NIMS), Tsukuba 305-0044, Japan

<sup>8</sup> Advanced Photon Source, Argonne National Laboratory, Argonne, Illinois 60439, USA

<sup>a</sup> Present address: HPCAT, Geophysical Laboratory, Carnegie Institution of Washington, Argonne, Illinois 60439, U.S.A.

<sup>b</sup> Present address: Laboratoire de Géologie de Lyon, Ecole Normale Supérieure de Lyon, Université Claude Bernard Lyon 1, CNRS UMR 5276, Lyon, France

24 <sup>c</sup> Present address: Hawaii Institute of Geophysics and Planetology, School of Ocean and  
25 Earth Sciences, University of Hawaii at Manoa, Honolulu, Hawaii 96822, U.S.A.

26 \* Corresponding author: [itaru.ohira@gmail.com](mailto:itaru.ohira@gmail.com)

27

28

## ABSTRACT

29 Hydrogen transport from the surface to the deep interior and distribution in the mantle  
30 are important in the evolution and dynamics of the Earth. An aluminum oxy-hydroxide,  
31  $\delta$ -AlOOH, likely influences the hydrogen transport process in the deep mantle because of  
32 its high stability extending to lower mantle conditions. The compressional behavior and  
33 spin states of  $\delta$ -(Al,Fe<sup>3+</sup>)OOH phases were investigated with synchrotron X-ray  
34 diffraction and Mössbauer spectroscopy under high pressure and room temperature.  
35 Pressure-volume ( $P$ - $V$ ) profiles of the  $\delta$ -(Al<sub>0.908(9)</sub><sup>57</sup>Fe<sub>0.045(1)</sub>)OOH<sub>1.14(3)</sub> (Fe/(Al+Fe) =  
36 0.047(10),  $\delta$ -Fe5) and the  $\delta$ -(Al<sub>0.832(5)</sub><sup>57</sup>Fe<sub>0.117(1)</sub>)OOH<sub>1.15(3)</sub> (Fe/(Al+Fe) = 0.123(2),  $\delta$ -  
37 Fe12) show that these hydrous phases undergo two distinct structural transitions  
38 involving changes in hydrogen bonding environments and a high- to low-spin crossover  
39 in Fe<sup>3+</sup>. A change of axial compressibility accompanied by a transition from ordered-  
40 ( $P2_1nm$ ) to disordered-hydrogen bond ( $Pnmm$ ) occurs near 10 GPa for both  $\delta$ -Fe5 and  $\delta$ -  
41 Fe12 samples. Through this transition, the crystallographic  $a$  and  $b$  axes become stiffer,  
42 whereas the  $c$  axis does not show such a change, as observed in pure  $\delta$ -AlOOH. A  
43 volume collapse due to a transition from high- to low-spin states in the Fe<sup>3+</sup> ions is  
44 complete below 32–40 GPa in  $\delta$ -Fe5 and  $\delta$ -Fe12, which is ~10 GPa lower than that  
45 reported for pure  $\epsilon$ -FeOOH. Evaluation of the Mössbauer spectra of  $\delta$ -  
46 (Al<sub>0.824(10)</sub><sup>57</sup>Fe<sub>0.126(4)</sub>)OOH<sub>1.15(4)</sub> (Fe/(Al+Fe) = 0.133(3),  $\delta$ -Fe13) also indicate a spin

47 transition between 32–45 GPa. Phases in the  $\delta$ -(Al,Fe)OOH solid solution with similar  
48 iron concentrations as those studied here could cause an anomalously high  $\rho/v_\Phi$  ratio  
49 (bulk sound velocity, defined as  $\sqrt{K/\rho}$ ) at depths corresponding to the spin crossover  
50 region (~900 to ~1000 km depth), whereas outside the spin crossover region a low  $\rho/v_\Phi$   
51 anomaly would be expected. These results suggest that  $\delta$ -(Al,Fe)OOH solid solution may  
52 be important in understanding the heterogeneous structure of the deep Earth.

53

54 **Keywords:**  $\delta$ -AlOOH,  $\delta$ -(Al,Fe)OOH, hydrous mineral, high-pressure, X-ray diffraction,  
55 Mössbauer spectroscopy, diamond anvil cell, synchrotron, water transport in the deep  
56 mantle

57

## 58 INTRODUCTION

59

60 Volatile transport, in particular hydrogen in the forms of water and hydroxyl, from the  
61 surface to the deep interior and distribution in the mantle are important in understanding  
62 the evolution and dynamics of the Earth. Important hosts of hydrogen in the deep mantle  
63 are hydrous and nominally-anhydrous minerals (e.g., Bell and Rossman 1992; Smyth and  
64 Jacobsen 2006; Ohtani 2005, 2015, Ohtani et al. 2016; Wirth et al. 2007; Pearson et al.  
65 2014; Kaminsky 2017; Tschauner et al. 2018). A dense aluminum oxy-hydroxide,  $\delta$ -  
66 AlOOH, likely plays a key role in hydrogen transport in the mantle transition zone and  
67 the lower mantle (e.g., Ohtani et al. 2016). This hydrous phase is a high-pressure  
68 polymorph of diaspore ( $\alpha$ -AlOOH) and boehmite ( $\gamma$ -AlOOH), and was first synthesized  
69 by Suzuki et al. (2000) at 21 GPa and 1273 K in a multi-anvil apparatus. High pressure  
70 and high temperature experiments using a multi-anvil apparatus and a laser heated

71 diamond anvil cell (DAC) combined with in situ X-ray diffraction (XRD) have  
72 demonstrated the stability of  $\delta$ -AlOOH at 21–142 GPa and 973–2410 K, corresponding to  
73 the conditions of the regions deeper than the lower transition zone (Sano et al. 2004,  
74 2008; Pamato et al. 2015; Fukuyama et al. 2017; Abe et al. 2018; Duan et al. 2018). This  
75 high stability implies that  $\delta$ -AlOOH has the potential to transport hydrogen to the core-  
76 mantle boundary (CMB) region.

77 The structure and physical properties of  $\delta$ -AlOOH at ambient and high pressure  
78 conditions have also been investigated. At ambient conditions,  $\delta$ -AlOOH has a distorted  
79 rutile-type structure with ordered (asymmetric) hydrogen bond ( $P2_1nm$ , off-centered  
80 hydrogen positions termed “HOC-I”) (Suzuki et al. 2000; Komatsu et al. 2006; Sano-  
81 Furukawa et al. 2009; Kuribayashi et al. 2014; Xue and Kanzaki 2007). During  
82 compression, the O $\cdots$ O distance ( $d_{OO}$ ) of  $\delta$ -AlOOH decreases, and this phase transforms  
83 from HOC-I to a proton-disordered symmetric structure characterized by proton  
84 tunneling ( $Pnmm$ , HOC-III) when the  $d_{OO}$  reaches the critical distance (2.439(6) Å) at 8  
85 GPa (Kuribayashi et al. 2014). High-pressure powder and single-crystal XRD  
86 measurements showed that this transition involves changes in axial compressibility  
87 (Sano-Furukawa et al. 2009; Kuribayashi et al. 2014), which are also supported by the  
88 recent computational studies (Cortona 2017; Kang et al. 2017; Pillai et al. 2018).

89 Further compression decreases the  $d_{OO}$ , and  $\delta$ -AlOOH adopts a proton-centered  
90 structure in which the  $d_{OO}$  is below  $\sim 2.366$  Å ( $Pnmm$ , HC) (Tsuchiya and Tsuchiya 2009).  
91 In our paper, the term of symmetrization indicates the transition to a proton-centered  
92 structure (i.e. the transition from HOC-III to HC). Because this symmetrization may  
93 cause a further increase in the bulk modulus, the determination of this transition pressure

94 is important to discuss the effect of  $\delta$ -phase on the seismic velocity in the lower mantle.  
95 However, computational studies using different approximations have shown conflicting  
96 pressure conditions for the symmetrization of  $\delta$ -AlOOH, ranging from 0 to 50 GPa  
97 (Cortona 2017; Panero and Stixrude 2004; Tsuchiya and Tsuchiya 2009; Tsuchiya et al.  
98 2002; Li et al. 2006; Cedillo et al. 2016; Bronstein et al. 2017; Kang et al. 2017; Pillai et  
99 al. 2018). On the other hand, sound wave velocity measurements using Brillouin  
100 spectroscopy demonstrated a precipitous increase by  $\sim 14\%$  in the sound velocities of  $\delta$ -  
101 AlOOH from 6 to 15 GPa (Mashino et al. 2016), and Raman spectroscopy results showed  
102 that the  $B_2$  mode peaks of  $P2_1nm$  broaden and disappear and the new peaks assigned to  
103 the  $A_g$  mode of  $Pnmm$  appear above 5.6 GPa (Mashino et al. 2016). Infrared spectra  
104 obtained from  $\delta$ -AlOOH also demonstrated the change of pressure dependence of  
105 hydrogen-based vibrational modes at 10 GPa (Kagi et al. 2010). The pressure conditions  
106 of symmetrization determined from the spectroscopic measurements are in the pressure  
107 range where changes in axial compressibility due to the occurrence of the order-disorder  
108 ( $P2_1nm$  HOC-I to  $Pnmm$  HOC-III) transition (Sano-Furukawa et al. 2009; Kuribayashi et  
109 al. 2014). Although the pressure conditions of hydrogen bond symmetrization remains  
110 unclear from the computational studies, the experimental data suggest that it would be  
111 completed at shallow lower mantle pressures (Sano-Furukawa et al. 2009; Kuribayashi et  
112 al. 2014; Mashino et al. 2016; Kagi et al. 2010). The recent neutron diffraction (ND)  
113 study on  $\delta$ -AlOOH by Sano-Furukawa et al. (2018) observed the order-disorder  
114 transition of the hydrogen bond at 9.0 GPa and the symmetrization at 18.1 GPa, and  
115 concluded that the discrepancy of symmetrization pressure between the experimental and

116 several computational studies is due to quantum and temperature effects, which was also  
117 suggested in the computational studies by Bronstein et al. (2017).

118  $\delta$ -AlOOH forms a solid solution with hydrous  $\text{MgSiO}_4\text{H}_2$  Phase H and  $\epsilon$ -FeOOH (a  
119 polymorph of goethite ( $\alpha$ -FeOOH)) phases because they also have  $P2_1nm$  and  $Pnmm$   
120 structures. Phase H has a proton-disordered symmetric structure ( $Pnmm$ , HOC-III) even at  
121 ambient conditions (Bindi et al. 2014), and it transforms to a proton-centered structure  
122 ( $Pnmm$ , HC) at around 30 GPa (Tsuchiya and Mookherjee 2015; Nishi et al. 2018).  $\epsilon$ -  
123 FeOOH phase has a proton-ordered asymmetric structure ( $P2_1nm$ , HOC-I) at ambient  
124 conditions (Pernet et al. 1975). Density functional theory (DFT) calculations on  $\epsilon$ -  
125 FeOOH predicted that hydrogen bond symmetrization (i.e., the transition to HC-structure)  
126 occurs at  $\sim 10$  GPa (Thompson et al. 2017) or  $\sim 43$  GPa (Gleason et al. 2013), and the  
127 high-spin to low-spin (HS–LS) spin transition occurs at 56.5 GPa (Otte et al. 2009) or  
128 64.8 GPa (Gleason et al. 2013). Hydrogen symmetrization pressure in  $\epsilon$ -FeOOH is higher  
129 than that in  $\delta$ -AlOOH predicted from DFT calculations ( $\sim 30$  GPa; Tsuchiya and Tsuchiya  
130 2009). However, it should be noted that the possible occurrence of a proton-disordered  
131 symmetric structure (HOC-III), which could appear at pressures lower than a proton-  
132 centered structure (HC), has not been evaluated in  $\epsilon$ -FeOOH. The HS–LS transition  
133 pressures in  $\epsilon$ -FeOOH predicted by theory are close to those determined with X-ray  
134 emission spectroscopy (40–60 GPa) and estimated from the volume collapse ( $\sim 46$ –54  
135 GPa) measured with XRD (Gleason et al. 2013).

136 The stability of hydrous  $\delta$ -phase– $\epsilon$ -FeOOH–Phase H solid solution has been confirmed  
137 up to at least 128 GPa and 2190 K in the  $\text{MgO}$ – $\text{Al}_2\text{O}_3$ – $\text{SiO}_2$ – $\text{H}_2\text{O}$  system (Ohira et al.  
138 2014; Walter et al. 2015). Ohira et al. (2014) reported the coexistence of bridgmanite

139 with minor Al ( $\text{MgSiO}_3$ –6 mol%  $\text{Al}_2\text{O}_3$ ) and Al-rich  $\delta$ -phase–Phase H solid solution  
140 containing about 40 mol% of a phase H component at 68 GPa and 2010 K. At 128 GPa  
141 and 2190 K, hydrous  $\delta$ -H solid solution coexisting with post-perovskite with minor Al  
142 ( $\text{MgSiO}_3$ –5 mol%  $\text{Al}_2\text{O}_3$ ) contains only 20 mol% of hydrous Phase H component (Ohira  
143 et al. 2014). A recent experimental study has shown a continuous chain of hydrous phases  
144 in cold oceanic crusts subducted from the Earth’s surface to the top of the lower mantle  
145 (Liu et al. 2019). In the hydrous basalt system,  $\epsilon$ -phase is formed as  $\epsilon$ -FeOOH– $\text{TiO}_2$  solid  
146 solution (Liu et al. 2019; Okamoto and Maruyama 2004), which is stable at 8–17 GPa  
147 and the cold slab temperatures (Liu et al. 2019; Okamoto and Maruyama 2004; Nishihara  
148 and Matsukage 2016). Then, the hydrous  $\delta$ -AlOOH– $\epsilon$ -FeOOH–phase H solid solution  
149 (referred to as “Al-rich Phase H” in Liu et al. 2019) is formed, and it coexists with  
150 bridgmanite,  $\text{CaSiO}_3$ -perovskite, stishovite, ferropericlase, and fluid at 25–26 GPa and  
151 1273–1473 K, comparable to the condition of cold slabs at the top of the lower mantle  
152 (Liu et al. 2019).

153 The composition of this hydrous phase formed in the hydrous basalt system is  
154  $\sim\text{Mg}_{0.11}\text{Si}_{0.20}\text{Al}_{0.63}\text{Fe}_{0.03}\text{O}_2\text{H}$ , (Liu et al. 2019), which is close to AlOOH end-member.  
155 Although the incorporation of  $\epsilon$ -FeOOH is limited, it might influence the physical  
156 properties of hydrous solid solution because Fe has large mass and might undergo the  
157 spin transition at lower mantle pressures. Therefore, the physical properties of  $\delta$ -AlOOH–  
158  $\epsilon$ -FeOOH ( $\delta$ -(Al,Fe)OOH) solid solution are important to understand the behavior of this  
159 hydrous solid solution under lower mantle conditions. However, the physical properties  
160 of  $\delta$ -(Al,Fe)OOH under lower mantle conditions have not been examined. To address



161 these issues, we have conducted a set of high-pressure XRD and synchrotron Mössbauer  
162 spectroscopy (SMS) experiments for  $\delta$ -(Al,Fe)OOH.

163

## 164 **EXPERIMENTAL METHODS**

165

### 166 **$\delta$ -(Al,Fe)OOH crystals**

167 The samples are selected from aggregates of single crystals of  $\delta$ -(Al,Fe)OOH phases  
168 synthesized with a hydrothermal method using a 1000-ton Kawai-type multi anvil  
169 apparatus installed at Bayerisches Geoinstitut, University of Bayreuth. The details of the  
170 synthesis and characterization of  $\delta$ -(Al,Fe)OOH under ambient conditions have been  
171 reported by Kawazoe et al. (2017). Therefore, we provide only a brief description here.

172 The single crystals of  $\delta$ -(Al,<sup>57</sup>Fe)OOH were synthesized at 21 GPa and 1470 K from a  
173 mixture of reagent-grade Al(OH)<sub>3</sub> (Rare Metallic Co., Ltd.) and Fe<sub>2</sub>O<sub>3</sub> (96.64% <sup>57</sup>Fe,  
174 ISOFLEX) using a Kawai-type multi-anvil apparatus. The initial dimensions of the  
175 recovered crystals were in the range of 0.1–0.5 mm. The chemical compositions and  
176 homogeneity of the  $\delta$ -(Al,Fe)OOH crystals were confirmed using an electron microprobe  
177 operating at 15 kV and 10 nA in the wavelength-dispersive mode (JEOL, JXA-8800,  
178 installed at Tohoku University). The oxide mass deficits of the synthesized samples were  
179 2–3 wt% greater than H<sub>2</sub>O contents which would be expected based on the H<sub>2</sub>O contents  
180 in their ideal chemical formulas, suggesting the incorporation of additional water  
181 (Kawazoe et al. 2017). In this study,  $\delta$ -(Al<sub>0.908(9)</sub><sup>57</sup>Fe<sub>0.045(1)</sub>)OOH<sub>1.14(3)</sub> (Fe/(Al+Fe) =  
182 0.047(10)) synthesized and  $\delta$ -(Al<sub>0.832(5)</sub><sup>57</sup>Fe<sub>0.117(1)</sub>)OOH<sub>1.15(3)</sub> (Fe/(Al+Fe) = 0.123(2)) were  
183 investigated with synchrotron XRD, and  $\delta$ -(Al<sub>0.824(10)</sub><sup>57</sup>Fe<sub>0.126(4)</sub>)OOH<sub>1.15(4)</sub> (Fe/(Al+Fe) =  
184 0.133(3)) with synchrotron Mössbauer spectroscopy (SMS) experiments. Hereafter, the

185 three samples are referred to as  $\delta$ -Fe5,  $\delta$ -Fe12, and  $\delta$ -Fe13, respectively. While  $\delta$ -Fe5 was  
186 selected from the crystals synthesized in the run H4473 in Kawazoe et al. (2017),  $\delta$ -Fe12  
187 and  $\delta$ -Fe13 were from the crystals synthesized in the run H4468 in that study. The  
188 additional sample for the single crystal XRD measurement at ambient conditions ( $\delta$ -  
189  $(\text{Al}_{0.807(7)}^{57}\text{Fe}_{0.117(4)})\text{OOH}_{1.15(3)}$  ( $\text{Fe}/(\text{Al}+\text{Fe}) = 0.127(3)$ , identical ratio to  $\delta$ -Fe12 within  
190 error) was also from the run H4468 (Kawazoe et al. 2017). The  $\text{Fe}/(\text{Al}+\text{Fe})$  ratios for the  
191 Fe-poor sample ( $\delta$ -Fe5) and the Fe-rich samples ( $\delta$ -Fe12 and  $\delta$ -Fe13) are identical to or  
192 slightly higher than that of  $\delta$ -phase formed at 25–26 GPa and 1273–1473 K in a hydrous  
193 oceanic crust ( $\sim\text{Mg}_{0.11}\text{Si}_{0.20}\text{Al}_{0.63}\text{Fe}_{0.03}\text{O}_2\text{H}$ , Liu et al. 2019).

194

#### 195 **XRD experiments**

196 The compression behavior of the  $\delta$ -(Al,Fe)OOH samples were examined with a  
197 membrane-type DAC (mDAC). This apparatus allowed the pressure in the sample  
198 chamber to be increased without unloading it from the X-ray path, thus reducing time  
199 interval between each measurement. Experimental pressure could be set precisely using  
200 the gas control system. Flat 300 and 250  $\mu\text{m}$ -culet diamonds were used as the anvils.  
201 Rhenium plates pre-indented to thicknesses of 50 and 47  $\mu\text{m}$  were used for the 300 and  
202 250  $\mu\text{m}$ -culet anvils, respectively, as gaskets. Crystals of  $\delta$ -(Al,Fe)OOH were powdered  
203 and then loaded into the sample hole in the gasket together with tungsten powder. One or  
204 two ruby spheres were placed proximal to the sample. Compressed helium gas was  
205 loaded into the sample chamber as the pressure medium at the National Institute for  
206 Materials Science (NIMS), Japan (Takemura et al. 2001).

207 Two sets of compression experiments were performed, using  $\delta$ -Fe12 (Run# DAF01)  
208 and  $\delta$ -Fe5 (Run# DAF02). In each run, XRD patterns were collected with the X-rays  
209 focused on the tungsten powder before and after each XRD pattern of the sample was  
210 collected. The pressure was determined using the equation of state (EoS) for tungsten  
211 (Dorogokupets and Oganov 2006), and the ruby fluorescence method (Dewaele et al.  
212 2008) was used to compare the pressure determined with the EoS for tungsten and to  
213 ensure quasi-hydrostatic conditions in the sample chamber. To avoid the overlapping of  
214 tungsten and  $\delta$ -(Al,Fe)OOH peaks, tungsten patterns were collected without the  $\delta$ -phase  
215 before and after each XRD measurement on the samples. The average pressure drift was  
216 0.3 GPa. The difference between the calculated pressures obtained using the EoS for  
217 tungsten and the ruby fluorescence method was less than 0.9 GPa in each case. The  
218 experimental pressures were increased up to 38 and 35 GPa in runs DAF01 and DAF02,  
219 respectively, by tightening the four screws on the mDAC. The pressure was subsequently  
220 increased to the maximum desired value by supplying helium gas to the unit. During the  
221 decompression process, the gas was first released followed by loosening of the screws. In  
222 the DAF02 experimental run, the ambient XRD pattern of  $\delta$ -Fe5 was collected after  
223 decompression. The ambient XRD patterns of the additional sample, the  $\delta$ -  
224  $(\text{Al}_{0.807(7)}^{57}\text{Fe}_{0.117(4)})\text{OOH}_{1.15(3)}$  ( $\text{Fe}/(\text{Al}+\text{Fe}) = 0.127(3)$ , identical ratio to  $\delta$ -Fe12 within  
225 error), were also collected at the X-ray Crystallography Facility in the Beckman Institute  
226 at the California Institute of Technology, where a Mo target ( $\lambda = 0.7107 \text{ \AA}$ ) was  
227 employed. The single crystal XRD analysis for the  $\delta$ -( $\text{Al}_{0.807(7)}^{57}\text{Fe}_{0.117(4)})\text{OOH}_{1.15(3)}$  under  
228 ambient conditions confirmed the structure of  $\delta$ -AlOOH under ambient conditions (e.g.,  
229 Suzuki et al. 2000) (space group as  $P2_1nm$ , the CIF file is in the deposit).

230 Angle dispersive powder XRD patterns were collected at the BL10XU beamline  
231 (Ohishi et al. 2008). An imaging plate (Rigaku, R-AXIS IV<sup>++</sup>) was used for acquiring the  
232 XRD patterns, and the exposure time was 8 min. The X-ray wavelength was 0.4141(1) Å  
233 (for compression and decompression in run# DAF01), 0.4152(2) Å (compression in run#  
234 DAF02) and 0.4143(1) Å (decompression in run# DAF02). One dimensional diffraction  
235 profiles were fitted with a pseudo-Voigt function using the PDIndexer software (Seto et  
236 al. 2010). The 110, 101, 011, 111, 210, 211, 121, 220, 310, 002, 301, and 112 reflections  
237 were employed to calculate the lattice parameters. The 101, 002, 211, 121, 220, 310, 301,  
238 and 112 reflections were excluded from the calculations when they overlapped with  
239 helium reflections. The 110, 211, and 220 reflections of tungsten were used for pressure  
240 determination (Dorogokupets and Oganov 2006). The determination method of lattice  
241 constants follows the previous study on Fe-free  $\delta$ -AlOOH (Sano-Furukawa et al. 2009) to  
242 compare the compressional behaviors of Fe-bearing and Fe-free  $\delta$ -phases. Pressure vs.  
243 unit cell volume ( $P$ - $V$ ) profiles obtained from the XRD experiments were fitted using a  
244 spin crossover EoS with version 2.1.0 of the MINUTI software (Sturhahn 2018).

245

#### 246 **Synchrotron Mössbauer spectroscopy experiments**

247 A wide-angled piston-cylinder DAC with 300  $\mu\text{m}$ -culet/370  $\mu\text{m}$ -beveled anvils was  
248 used to generate high pressure conditions for the SMS experiments. A piece of  $\delta$ -Fe13  
249 with dimensions of  $40 \times 50 \times 20 \mu\text{m}$  was cut from a larger crystallite in the same  
250 synthesis run described above. A beryllium disk pre-indented to a thickness of 38  $\mu\text{m}$  was  
251 used as a gasket. The diameter of the sample hole in the gasket was 165  $\mu\text{m}$  for 300  $\mu\text{m}$ -  
252 culet anvils. A mixture of 10–20  $\mu\text{m}$  thick boron epoxy (amorphous boron powder:epoxy

253 = 4:1 by weight; Lin et al. 2003) was put on the side of a beryllium gasket hole. Two  
254 ruby spheres were positioned beside the sample as pressure markers (Dewaele et al.  
255 2008). Compressed neon gas was loaded into the sample chamber as a pressure medium  
256 at the California Institute of Technology.

257 Time-domain SMS measurements were conducted on a single crystal of  $\delta$ -Fe<sub>13</sub> at  
258 Sector 3-ID-B at the Advanced Photon Source (APS). The storage ring was operated in  
259 top-up mode with 24 bunches separated by 153 ns. A high-resolution monochromator  
260 was tuned to the 14.4125 keV nuclear transition energy of <sup>57</sup>Fe with a FWHM of about 1  
261 meV (Toellner 2000). The beam was focused to an area of 10 by 14  $\mu\text{m}^2$  using a  
262 Kirkpatrick-Baez mirror system. The time spectra were measured with an avalanche  
263 photodiode detector positioned about 0.5 m downstream from the sample. A 10  $\mu\text{m}$  thick  
264 stainless steel (SS) foil with a natural abundance of <sup>57</sup>Fe was placed in the downstream  
265 direction as a reference absorber for isomer shift measurements. At each compression  
266 point, a spectrum was collected of the sample with and without the SS reference foil. The  
267 isomer shift between the SS foil and  $\alpha$ -iron metal was measured at the APS using a  
268 radioactive source and found to be  $-0.100(3)$  mm/s with a corresponding FWHM (due to  
269 the effect of site distribution ) of  $0.445(9)$  mm/s (Solomatova et al. 2017).

270 Synchrotron Mössbauer spectra were fitted with version 2.1.1 of the CONUSS  
271 software (Sturhahn 2000, 2016), which implements a least-square algorithm to fit iron's  
272 hyperfine parameters and material properties. The spectrum of the sample and sample  
273 with SS were fitted simultaneously. For a single crystal, the orientation of the electric  
274 field gradient tensor of each iron site must be specified with respect to the direction and  
275 polarization of the X-ray using three Euler angles ( $\alpha$ ,  $\beta$  and  $\gamma$ ). The orientation of the

276 crystal was determined through careful analysis of the reduced  $\chi^2$  and Monte Carlo  
277 searches. The Euler angles of the high-spin site were calculated using the CONUSS  
278 module, “kvzz” using the lattice parameters and atomic positions of  $\delta$ -Fe13. The Euler  
279 angles for the low-spin sites were determined through a Monte Carlo search and were  
280 fixed with pressure.

281

282

## RESULTS

283

### 284 XRD experiments

285  $\delta$ -Fe12 ( $\delta$ -(Al<sub>0.832(5)</sub><sup>57</sup>Fe<sub>0.117(1)</sub>)OOH<sub>1.15(3)</sub>, Run# DAF01) and  $\delta$ -Fe5 ( $\delta$ -  
286 (Al<sub>0.908(9)</sub><sup>57</sup>Fe<sub>0.045(1)</sub>)OOH<sub>1.14(3)</sub>, Run# DAF02) were compressed to 65 and 56 GPa,  
287 respectively. The representative one-dimensional XRD patterns of the samples converted  
288 from two-dimensional patterns are shown in Figure 1. The lattice constants ( $a$ ,  $b$ , and  $c$ )  
289 and unit cell volumes determined from the XRD data for  $\delta$ -Fe12 and  $\delta$ -Fe5 are  
290 summarized in Tables 1 and 2, respectively. It should be noted that the tungsten pressure  
291 scale does not include the errors of EoS parameters ( $V_0$ ,  $K_0$ ,  $K'$ ), and therefore the  
292 experimentally determined pressures in this study might be relatively smaller than the  
293 other experimental studies (e.g., Duan et al. 2018). A potential pressure error might be up  
294 to ~2%, as presumed in Sano-Furukawa et al. (2009).

295 Figure 2 shows the  $P$ - $V$  profiles of the two samples during compression and  
296 decompression. The unit cell volume obtained during decompression is plotted along  
297 with the compressional profiles (Fig. 2). The  $P$ - $V$  profiles of  $\delta$ -Fe12 and  $\delta$ -Fe5 show that  
298 both  $\delta$ -(Al,Fe)OOH phases undergo multiple structural transitions over the experimental  
299 pressure ranges, related to the change of the hydrogen bonds (e.g., Sano-Furukawa et al.

300 2008, 2009, 2018; Kuribayashi et al. 2014) and spin transition in  $\text{Fe}^{3+}$  (Gleason et al.  
301 2013; Otte et al. 2009). The associated characteristics are:

302 (1) asymmetric (ordered) hydrogen bonds + high-spin state (HOC-I-HS, space group  
303  $P2_1nm$ )

304 (2) symmetric hydrogen bonds + high-spin state (HS,  $Pnmm$ )

305 (2a) symmetric (disordered) hydrogen bonds + high-spin state (HOC-III-HS,  $Pnmm$ )

306 (2b) symmetric (proton-centered) hydrogen bonds + high-spin state (HC-HS,  $Pnmm$ )

307 (3) symmetric hydrogen bonds + low-spin state (LS,  $Pnmm$ ).

308 It should be noted that the HOC-III-HS (2a) and HC-HS (2b) states cannot be  
309 distinguished in the XRD data, as discussed in the previous studies regarding pure  $\delta$ -  
310  $\text{AlOOH}$ . This is because the former structure (2a) has two crystallographically equivalent  
311 hydrogen sites characterized by proton tunneling and further transition to (2b) does not  
312 involve a detectable change in compressibility. For example, the recent ND experiment  
313 on  $\delta$ - $\text{AlOOH}$  provided direct evidence that the order–disorder transition of the hydrogen  
314 bond and the symmetrization occur at different pressure conditions (9.0 and 18.1 GPa,  
315 respectively), and argued the importance of the hydrogen bond disorder as a precursor of  
316 the symmetrization in understanding the physical properties of minerals under high  
317 pressures (Sano-Furukawa et al. 2018). Therefore, the possible transition from HOC-III-  
318 HS to HC-HS before the onset of HS–LS transition is not evaluated in this study.

319 The  $P2_1nm$ (HOC-I)-HS (1) and  $Pnmm$ (HOC-III)-HS (2a) states are separated by the  
320 subtle kinks in the  $P$ - $V$  profiles (Fig. 2) and the inversion of axial compressibility at  $\sim 10$   
321 GPa (Fig. 3).  $Pnmm$ -HS (2) and  $Pnmm$ -LS (3) are distinguished by a volume collapse at  
322  $\sim 32$ – $40$  GPa (Fig. 2). Profiles of normalized pressure ( $F$ ) against Eulerian strain ( $f$ ) also

323 demonstrate changes in compressibility that occur through the symmetrization of  
324 hydrogen bonds and spin crossover (Fig. 4).

325 A second-order Birch-Murnaghan (BM) EoS was fitted to the  $P$ - $V$  profiles of  $\delta$ -Fe12  
326 and  $\delta$ -Fe5 with the  $P2_1nm$  structure, while a third-order Birch-Murnaghan spin crossover  
327 EoS (hereafter, spin crossover EoS) was fitted to the  $P$ - $V$  profiles of  $\delta$ -Fe12 and  $\delta$ -Fe5  
328 with the  $Pnmm$  structure using the MINUTI software (Sturhahn 2018) (Fig. 5 and Table  
329 3). We consider the elastic and spin state (i.e.,  $3d$  electrons of the Fe atoms) contributions  
330 to the free energy of the sample. For the elastic contribution, we adopt an expression  
331 corresponding to the commonly-used third-order Birch-Murnaghan EoS (3rd-order BM  
332 EoS)

$$333 \quad F_{\text{elastic}} = \frac{9}{2} V_{T0} K_{T0} f^2 \{1 + (K'_{T0} - 4)f\}, \quad (1)$$

334 where the Eulerian strain is given by  $f = \{(V_0/V)^{2/3} - 1\}/2$ , and  $V_0$ ,  $K_{T0}$ , and  $K'_{T0}$  are the  
335 unit cell volume, isothermal bulk modulus, and the pressure derivative of  $K_{T0}$  at room  
336 temperature, respectively. The Eq. 1 with a fixed  $K'_{T0}$  of 4 is called as 2nd-order BM EoS.  
337 For the spin contribution, we assume a set of spin states described by the number of  
338 unpaired electron, volume-dependent energy, and orbital degeneracy. For a given  
339 pressure  $P$ , the volume at room temperature is calculated by solving the spin crossover  
340 EoS

$$341 \quad P(V, 300 \text{ K}) = P_{\text{elastic}}(V, 300 \text{ K}) + P_{\text{spin}}(V, 300 \text{ K}). \quad (2)$$

342 For more details of the spin crossover EoS, we refer the reader to Chen et al. (2012) and  
343 Sturhahn (2018).

344 A spin crossover EoS reproduces the behavior of  $\delta$ -Fe12 and  $\delta$ -Fe5 in the crossover  
345 region (Fig. 5 and Table 3). The pressure condition where the unit cell volume changes



346 due to the HS–LS transition is 50% complete is determined for  $\delta$ -Fe12 at  $36.1 \pm 0.7$  GPa,  
347 which is defined as the spin transition pressure. Although the volume collapse of  $\delta$ -Fe5 is  
348 very small due to the low  $\text{Fe}^{3+}$  content in the sample, it was nonetheless possible to  
349 determine the spin transition pressure of  $34.9 \pm 1.1$  GPa. The values of  $F$  were found to  
350 decrease with increasing  $f$  through the spin crossover, which is seen clearly in both the  
351 Fe-rich  $\delta$ -Fe12 and the Fe-poor  $\delta$ -Fe5 samples (Fig. 4). The isothermal bulk modulus ( $K_T$ )  
352 and bulk sound velocity ( $v_\Phi$ ) of  $\delta$ -Fe12 and  $\delta$ -Fe5 also decrease in the spin crossover  
353 (Fig. 6).

354

### 355 **SMS experiments**

356 Synchrotron Mössbauer spectra of  $\delta$ -Fe13 were collected at 21.1(2), 31.8(8), 45(2),  
357 59(2), 67.5(5), and 78.6(5) GPa (Fig. 7). The results of SMS experiments demonstrate  
358 that the HS–LS transition in  $\delta$ -Fe13 is completed by 45 GPa (Fig. 8), which is similar to  
359 the pressure conditions at which volume collapse is completed in the  $P$ - $V$  profiles of  $\delta$ -  
360 Fe12 and  $\delta$ -Fe5. At 21.1 and 31.8 GPa, one high-spin  $\text{Fe}^{3+}$ -like site was required to fit the  
361 spectra with a quadrupole splitting value of  $\sim 0.4$  mm/s and isomer shift of 0.2 mm/s, thus  
362 we find that 100% of the iron in this phase is  $\text{Fe}^{3+}$  (see Figs. 7 and 8, and Table 4, which  
363 include reported uncertainties).

364 We attempted to fit the spectra above 32 GPa with one low-spin site, but the best  
365 model with one low-spin site resulted in a reduced  $\chi^2$  of 5. Although  $\delta$ -Fe13 is  
366 characterized by one crystallographic Fe site, the Mössbauer spectra above 32 GPa  
367 require two distinct nuclear sites. It is possible that the crystal quality decreased and/or  
368 next nearest neighbor interactions explain the additional Mössbauer-site. At pressures of

369 45 GPa and higher, the two low-spin Fe<sup>3+</sup>-like sites are characterized as follows: one with  
370 a quadrupole splitting value of ~1.14–1.32 mm/s and a second site with a quadrupole  
371 splitting value of 1.73–2.01 mm/s with weight fractions of 67% and 33%, respectively  
372 (Figs. 7 and 8, and Table 4). The isomer shifts with values 0.107–0.249 mm/s follow a  
373 negative trend with pressure indicating an increase of the s-electron density at the iron  
374 sites that is probably caused by volume decrease.

375 For all evaluations of the time spectra, we assumed axial symmetry of the electric field  
376 gradient tensor at the iron sites. Therefore, only two Euler angles,  $\alpha$  and  $\beta$ , need to be  
377 considered. For the HS site, these Euler angles were calculated from the lattice  
378 parameters and atomic positions of this phase (Table 5). For the LS sites  $\alpha$  and  $\beta$  were  
379 determined from a Monte Carlo search resulting in values of 296° and 261° for one of the  
380 LS sites and 22° and 253° for the other site, respectively.

381

382

## DISCUSSION

383 Subtle kinks in the  $P$ - $V$  profiles for  $\delta$ -Fe12 and  $\delta$ -Fe5 are observed at approximately 10  
384 GPa (Fig. 2), which may be a result of a structural transition from ordered ( $P2_1nm$ (HOC-  
385 I)-HS) to disordered hydrogen bonds ( $Pnmm$ (HOC-III)-HS), as observed in XRD and ND  
386 measurements on pure  $\delta$ -AlOOH (Sano-Furukawa et al. 2009, 2018; Kuribayashi et al.  
387 2014). The  $a/c$  and  $b/c$  values decrease rapidly with increasing pressure below ~10 GPa,  
388 whereas the  $a/b$  values increase up to ~10 GPa. The trend in the axial compressibility is  
389 reversed above 10 GPa such that the  $a$  and  $b$  axes are less compressible than the  $c$  axis  
390 (Fig. 3). Our finding that the  $a$  and  $b$  axes are less compressible than the  $c$ -axis above 10  
391 GPa are corroborated by computational studies for pure  $\delta$ -AlOOH showing that the

392 hydrogen bonds in the *Pnmm* structure are stronger than those in the *P2<sub>1</sub>nm* phase  
393 (Cortona 2017; Tsuchiya and Tsuchiya 2009; Tsuchiya et al. 2002; Kang et al. 2017;  
394 Pillai et al. 2018). Such an inversion of the compressibility is also observed in  $\delta$ -AlOOH  
395 at 8–10 GPa (Sano-Furukawa et al. 2009, 2018; Kuribayashi et al. 2014). The hydrogen  
396 bonds in the *Pnmm* structures are almost parallel to the  $\langle 120 \rangle$  direction, so the effects of  
397 these hydrogen bonds on structures and physical properties are stronger along the *b* axis  
398 than the *a* axis (Kuribayashi et al. 2014), while the compressibility of the *c* axis is  
399 unlikely to be modified. The pressure conditions of inversions of compressibility in  $\delta$ -  
400 Fe12 and  $\delta$ -Fe5 are very close to that of pure  $\delta$ -AlOOH (Sano-Furukawa et al. 2009,  
401 2018; Kuribayashi et al. 2014). Our data demonstrates that Fe incorporation into the  $\delta$ -  
402 phase is insensitive to the pressure condition of *P2<sub>1</sub>nm* (ordered-hydrogen bond)–*Pnmm*  
403 (disordered hydrogen bond) transition.

404 The SMS experiments show that octahedrally-coordinated Fe<sup>3+</sup> in  $\delta$ -Fe13 undergoes a  
405 HS–LS transition at the pressure range of 32–45 GPa. Collapse in unit cell volume is also  
406 observed in the  $\delta$ -Fe12 and  $\delta$ -Fe5 samples within this pressure range, likely as a result of  
407 the Fe<sup>3+</sup> spin transition. The spin-crossover pressures estimated from the *P-V* profiles of  
408  $\delta$ -Fe12 and  $\delta$ -Fe5 are within the pressure range of ~32–40 GPa, which is ~10 GPa lower  
409 than that of  $\epsilon$ -FeOOH examined with XRD experiments (46–54 GPa, Gleason et al.  
410 2013), suggesting that the LS state would be stabilized at lower pressures with decreasing  
411 FeOOH concentration in the solid solution. The positive correlation between Fe content  
412 and spin-transition pressure has also been reported for the MgO (periclase)–FeO (wüstite)  
413 solid solution. The spin-transition pressure of Fe<sup>2+</sup> in (Mg,Fe)O is reduced with  
414 decreasing FeO content (e.g., Lin et al. 2005; Fei et al. 2007; Solomatova et al. 2016).

415 Our results demonstrate that this relationship also applies to the  $\delta$ -AlOOH– $\epsilon$ -FeOOH  
416 solid solution.

417 The spin transition in  $\text{Fe}^{3+}$  is also observed in the new hexagonal aluminous phase  
418 (NAL phase). NAL phase has the chemical formula of  $\text{AB}_2\text{C}_6\text{O}_{12}$  ( $\text{A} = \text{Na}^+, \text{K}^+, \text{Ca}^{2+}$ ;  $\text{B} =$   
419  $\text{Mg}^{2+}, \text{Fe}^{2+}, \text{Fe}^{3+}$ ;  $\text{C} = \text{Al}^{3+}, \text{Si}^{4+}, \text{Fe}^{3+}$ ) with the space group of  $P6_3/m$  (Gasparik et al.  
420 2000; Miura et al. 2000; Miyajima et al. 2001), and is considered to exist in a basaltic  
421 layer of the slab subducted to the upper region of the lower mantle (e.g., Irifune and  
422 Ringwood 1993). The recent experimental study under room temperature reported that  
423 the Fe-bearing ( $\text{Na}_{0.71}\text{Mg}_{2.05}\text{Fe}^{2+}_{0.09}\text{Al}_{4.62}\text{Fe}^{3+}_{0.17}\text{Si}_{1.16}\text{O}_{12}$ ) NAL phase showed 1.0%  
424 volume reduction at 33–47GPa associated with the Fe spin transition (Wu et al. 2016). In  
425 the NAL phase, only  $\text{Fe}^{3+}$  in the octahedral C site undergoes the spin transition at the  
426 pressure conditions of the upper region of lower mantle, while  $\text{Fe}^{2+}$  and  $\text{Fe}^{3+}$  in the  
427 trigonal-prismatic B site maintain high-spin states up to at least 80 GPa (Wu et al. 2016;  
428 Hsu 2017). Therefore, only  $\text{Fe}^{3+}$  in the octahedral site contributes to the spin transition in  
429 NAL phase at that pressure range, which could explain why the width of the spin  
430 crossover where the softening occurs is slightly narrower in  $\delta$ -(Al,Fe)OOH samples (Fig.  
431 9).

432 It should be noted that a HOC-III–HC transition without an observable change in the  
433  $P$ - $V$  compression trend may occur in the  $\delta$ -(Al,Fe)OOH samples before or concurrently  
434 with the spin crossover, because the HOC-III–HC transition pressure of  $\delta$ -AlOOH is ~20  
435 GPa (Sano-Furukawa et al. 2018) and for  $\epsilon$ -FeOOH it ranges from ~10 to ~43 GPa  
436 (Thompson et al. 2017; Gleason et al. 2013), respectively. Further studies are required to

437 investigate the relationship between hydrogen symmetrization and spin state in the  $\delta$ -  
438  $\text{AlOOH}$ - $\epsilon$ - $\text{FeOOH}$  solid solution.

439

440

## IMPLICATIONS

441 In hydrous rock systems,  $\delta$ - $\text{AlOOH}$  may form a solid solution with isostructural  
442  $\text{MgSiO}_4\text{H}_2$  Phase H (Suzuki et al. 2000; Ohtani et al. 2001; Nishi et al. 2014, 2015; Ohira  
443 et al. 2014; Walter et al. 2015; Panero and Caracas 2017; Liu et al. 2019) and  $\epsilon$ - $\text{FeOOH}$   
444 components (Nishi et al. 2015, 2017; Kawazoe et al. 2017; Liu et al. 2019). Therefore,  
445 the incorporation of MgSi- and Fe-endmember components into the  $\delta$ -phase would need  
446 to be considered in interpretations of lower mantle seismic observations. However, Nishi  
447 et al. (2018) found that the incorporation of a Phase H component into the  $\delta$ -phase has  
448 little effect on the density of the  $\delta$ -phase because the differences of volume and mole  
449 weight between  $\delta$ - $\text{AlOOH}$  and  $\text{MgSiO}_4\text{H}_2$  Phase H are only 1.0–1.2% and 1.3% at the  
450 pressure condition from top- to mid-lower mantle. Therefore, the physical properties of  
451 binary  $\delta$ - $\text{AlOOH}$ - $\epsilon$ - $\text{FeOOH}$  solid solution, investigated in this study, are important to  
452 understand the behavior of ternary  $\delta$ - $\text{AlOOH}$ - $\epsilon$ - $\text{FeOOH}$ -phase H solid solution under  
453 lower mantle conditions.

454 Figure 9 shows the isothermal bulk modulus, density, bulk sound velocity, and the  
455 ratio of density to bulk sound velocity for  $\delta$ -Fe12,  $\delta$ -Fe5, several hydrous phases, and Fe-  
456 bearing NAL phase at pressures between the top- and mid-lower mantle. Our results  
457 show that the isothermal bulk modulus of low-spin  $\delta$ -Fe12 is larger than those of  $\delta$ -  
458  $\text{AlOOH}$ ,  $\text{MgSiO}_4\text{H}_2$  Phase H, and  $\epsilon$ - $\text{FeOOH}$ , and that of low-spin  $\delta$ -Fe5 is comparable to  
459 that reported for  $\delta$ - $\text{AlOOH}$  and  $\epsilon$ - $\text{FeOOH}$ , except for the pressure conditions of the spin

460 crossover (Fig. 9a). DFT calculations suggest that the bulk modulus of low-spin  $\epsilon$ -  
461 FeOOH is 4–8 % higher than the bulk modulus of  $\delta$ -AlOOH at pressures of the entire  
462 lower mantle and 0 K (Thompson et al. 2017). Interestingly, although the bulk modulus  
463 trends of  $\delta$ -Fe12 and  $\delta$ -Fe5 overlap within error (see Fig. 6), the values for the Fe-rich  $\delta$ -  
464 Fe12 sample are systematically 2–3 % higher than those of the Fe-poor  $\delta$ -Fe5 sample  
465 above 45 GPa in spite of an only  $\sim 7$  at% difference in Fe content. Therefore, our results  
466 suggest that the bulk modulus of low spin  $\delta$ -(Al,Fe)OOH may be sensitive to smaller  
467 amounts of Fe incorporation than the computational study predicted (Thompson et al.  
468 2017). This sensitive relationship between the bulk modulus and Fe content  $\delta$ -  
469 (Al,Fe)OOH may influence in understanding the origin of seismic anomalies in the lower  
470 mantle. The  $\rho$ ,  $v_{\Phi}$ , and their ratio ( $\rho/v_{\Phi}$ ) of pure  $\delta$ -AlOOH were calculated along a mantle  
471 geotherm (Brown and Shankland, 1981) to be 11–12% lower, 5–8% higher, and 16–18%  
472 lower than those of PREM, respectively, implying that the low  $\rho/v_{\Phi}$  ratio of pure  $\delta$ -  
473 AlOOH can help identify its potential presence in the lower mantle (Duan et al. 2018).  
474 The incorporation of Fe into  $\delta$ -(Al,Fe)OOH decreases the gaps of these properties  
475 between  $\delta$ -phase and PREM, due to the relatively large mass of Fe. Nevertheless,  $\delta$ -Fe12  
476 and  $\delta$ -Fe5 samples still exhibit higher  $v_{\Phi}$  and lower  $\rho$  and  $\rho/v_{\Phi}$  ratio, compared to PREM.  
477 Therefore, a low  $\rho/v_{\Phi}$  anomaly caused by the presence of an iron-bearing  $\delta$ -phase likely  
478 occurs in the lower mantle, with the exception of the spin crossover region.

479 If subducting materials including the hydrous solid solution are transported to the  
480 lower mantle, this hydrous phase might accumulate in deep lower mantle regions over  
481 geologic time. Continuous transport of subducted slab material to the deep lower mantle  
482 has been supported by geophysical simulations and geochemical studies (e.g., Tackley

483 2011; Bower et al. 2011; van der Meer et al. 2010). One of the possible contributions of  
484 the hydrous  $\delta$ -AlOOH- $\epsilon$ -FeOOH-phase H solid solution is a high- $v_{\Phi}$  anomaly in the  
485 lower mantle. For example, the approximately 0.3%  $v_{\Phi}$  increase is observed at the  
486 boundary regions of large low shear velocity provinces (Masters et al. 2000). Those  
487 provinces are located at a depth of  $\sim$ 2,000–2,890 km beneath the Pacific Ocean and the  
488 Atlantic Ocean—the western and southern part of the African continent, and are adjacent  
489 to the path of a subducting slab. If we apply the thermal parameters of  $\delta$ -AlOOH reported  
490 by Duan et al. (2018) to  $\delta$ -Fe5 or  $\delta$ -Fe12, this anomaly can be explained by the  
491 accumulation of  $\sim$ 6–8 wt%  $\delta$ -Fe5 or  $\delta$ -Fe12, which is  $\sim$ 9% lower than the proportion of  
492 hydrous  $\delta$ -AlOOH- $\epsilon$ -FeOOH-phase H solid solution ( $\delta$ -(Mg<sub>0.11</sub>Fe<sub>0.03</sub>Si<sub>0.2</sub>Al<sub>0.63</sub>)OOH,  
493 termed as “Al-rich Phase H” in Liu et al. 2019) formed in the oceanic basalt + 3.5 wt.%  
494 H<sub>2</sub>O system (Liu et al. 2019). The accumulation of  $\sim$ 6–8 wt%  $\delta$ -Fe5 or  $\delta$ -Fe12 is  
495 equivalent to the presence of only  $\sim$ 1 wt% H<sub>2</sub>O.

496 The low  $\rho/v_{\Phi}$  character of  $\delta$ -(Al,Fe)OOH becomes inverted to a high  $\rho/v_{\Phi}$  within the  
497 spin crossover due to the softening of the bulk modulus (Figs. 6 and 9). Although the spin  
498 transition of Fe<sup>3+</sup> in the octahedral site is also observed in the Fe-bearing NAL phase, the  
499 transition pressure is lower and the width of spin crossover is slightly narrower in the  $\delta$ -  
500 (Al,Fe)OOH samples than the Fe-bearing NAL phase (Wu et al. 2016). The spin  
501 crossover and resultant softening are influenced by temperature and valance of Fe. For  
502 example, the onset pressure for the LS state in (Mg<sub>0.75</sub>Fe<sub>0.25</sub>)O ferropericlaase increases  
503 from  $\sim$ 50 GPa at 300 K to 65 GPa at 1200 K, with an appreciable increase in the width of  
504 the spin crossover region (e.g., Mao et al. 2011). On the other hand, a computational  
505 study by Hsu (2017) showed that the spin transition pressure of Fe<sup>3+</sup> in the octahedral site

506 of the NAL phase (~40 GPa) remains mostly invariant to temperature and the width  
507 moderately increases with temperature. This would imply that for  $\delta$ -(Al,Fe)OOH at 1200  
508 K, the estimated temperature of a subducted slab at the top of the lower mantle (Ricard et  
509 al. 2005; Kirby et al. 1996), the spin transition pressure will likely be unchanged from  
510 that measured at 300 K and the softening of bulk modulus remains appreciable. The spin  
511 transition pressure and the width of spin crossover are slightly lower and narrower in the  
512  $\delta$ -(Al,Fe)OOH samples than the Fe-bearing NAL phase (Fig. 9). Therefore, the high  $\rho/v_\phi$   
513 of  $\delta$ -(Al,Fe)OOH in the spin crossover region would be observable at the pressure  
514 conditions of the uppermost lower mantle, especially under relatively cooler  
515 temperatures, such as those calculated for a subducted slab. Seismological studies have  
516 reported the laterally heterogeneous  $\rho$  and  $v_\phi$  in the upper region of the lower mantle  
517 (Masters et al. 2000; Trampert et al. 2004), and the presence of  $\delta$ -(Al,Fe)OOH may  
518 explain these anomalies.

519 In this section, we have focused on drawing comparisons of our results for the  $\delta$ -  
520 (Al,Fe)OOH solid solution across the spin transition, with those of endmember phases ( $\delta$ -  
521 AlOOH,  $\epsilon$ -FeOOH, and MgSiO<sub>4</sub>H<sub>2</sub> Phase H), the Fe-bearing NAL phase, and PREM. We  
522 have also suggested that  $\delta$ -(Al,Fe)OOH could cause low  $\rho/v_\phi$  anomaly in the lower  
523 mantle, except for the conditions where the spin crossover occurs. Specifically,  $\delta$ -  
524 (Al,Fe)OOH has high  $\rho/v_\phi$  ratio due to the spin crossover, which occurs under uppermost  
525 lower mantle conditions. These anomalies in geophysical properties of  $\delta$ -(Al,Fe)OOH  
526 suggest that the presence of  $\delta$ -(Al,Fe)OOH could be detectable and provide new insight  
527 for understanding the heterogeneity in the lower mantle.

528



## ACKNOWLEDGMENTS

529

530

531

532

533

534

535

536

537

538

539

540

541

542

543

544

545

546

547

548

549

550

551

552

We thank Y. Ito for his help with polishing or the EPMA-analyzing for the crystals used in this work. We also thank R. Njul for his help with polishing for a part of the samples. We are grateful to the editor D. Hummer and two anonymous reviewers for comments that helped to improve the manuscript. This work was supported by a Grant-in-Aid for Scientific Research from the Ministry of Education, Culture, Science, Sport and Technology of the Japanese Government to I.O. (JSPS KAKENHI Grant Number: JP16J04690), to E.O. (Number: JP15H05748), to S.K. (Number: 26247089, 15H05831, and 16K13902), to A.S. (Number: JP15H05828 and JP19H01985). This work and I.O. were supported by the International Research and Training Group “Deep Earth Volatile Cycles” funded by the German Science Foundation (grant number: GRK 2156/1), the JSPS Japanese-German Graduate Externship, and the International Joint Graduate Program in Earth and Environmental Science (GP-EES), Tohoku University. This work was also partially supported by a grant from the W.M. Keck Institute for Space Studies and the National Science Foundation (NSF-CSEDI-EAR-1600956) awarded to J.M.J. N.V.S. was partly funded by the European Research Council (ERC) under the European Union’s Horizon 2020 research and innovation program (grant agreement number 681818 – IMPACT). XRD measurements were performed at the BL10XU, SPring-8, Japan (proposal number: 2017A1650 to I.O., 2017A1251 to S.K., 2017A1673 to F.M., and 2015B0104, 2016A0104, and 2017B1514 to E.O.). SMS experiments were conducted at 3-ID-B, Advanced Photon Source, the United States, which is partially supported by COMPRES.

553

554

## REFERENCES CITED

555

556 Abe, R., Shibazaki, Y., Ozawa, S., Ohira, I., Tobe, H., and Suzuki, A. (2018) In situ X-

557

ray diffraction studies of hydrous aluminosilicate at high pressure and

558

temperature. *Journal of Mineralogical and Petrological Sciences*, 113, 106–111.

559

Bell, D.R., and Rossman, G.R. (1992) Water in Earth's mantle: the role of nominally

560

anhydrous minerals. *Science*, 255, 1391–1397.

561

Bindi, L., Nishi, M., Tsuchiya, J., and Irifune, T. (2014) Crystal chemistry of dense

562

hydrous magnesium silicates: The structure of Phase H,  $\text{MgSiH}_2\text{O}_4$  synthesized at

563

45 GPa and 1000 °C. *American Mineralogist*, 99, 1802–1805.

564

Bower, D.J., Gurnis, M., and Seton, M. (2011) Lower mantle structure from

565

paleogeographically constrained dynamic Earth models. *Geochemistry*

566

*Geophysics Geosystems*, 14, 44–63.

567

Bronstein, Y., Depondt, P., and Finocchi F. (2017) Thermal and nuclear quantum effects

568

in the hydrogen bond dynamical symmetrization phase transition of  $\delta\text{-AlOOH}$ .

569

*European Journal of Mineralogy*, 29, 385–395.

570

Brown, J.M., and Shankland, T.J. (1981) Thermodynamic parameters in the Earth as

571

determined from seismic profiles. *Geophysical Journal of the Royal Astronomical*

572

*Society*, 66, 579–596.

573

Cedillo, A., Torrent, M., and Cortona, P. (2016) Stability of the different  $\text{AlOOH}$  phases

574

under pressure. *Journal of Physics: Condensed Matter*, 28, 185401.

575

Chen, B., Jackson, J.M., Sturhahn, W., Zhang, D., Zhao, J., Wicks, J.K., and Murphy,

576

C.A. (2012) Spin crossover equation of state and sound velocities of

577 (Mg<sub>0.65</sub>Fe<sub>0.35</sub>)O ferropericlase to 140 GPa. *Journal of Geophysical Research*, 117,  
578 B08208.

579 Cortona, P. (2017) Hydrogen bond symmetrization and elastic constants under pressure  
580 of  $\delta$ -AlOOH. *Journal of Physics: Condensed Matter*, 29, 325505.

581 Dewaele A., Torrent, M., Loubeyre, P., and Mezouar, M. (2008) Compression curves of  
582 transition metals in the Mbar range: Experiments and projector augmented-wave  
583 calculations. *Physical Review B*, 78, 104102.

584 Dorogokupets, P.I., and Oganov, A.R. (2006) Equations of state of Al, Au, Cu, Pt, Ta,  
585 and W and revised ruby pressure scale. *Doklady Earth Sciences*, 410, 1091–1095.

586 Duan, Y., Sun, N., Wang, S., Li, X., Guo, X., Ni, H., Prakapenka, V.B., and Mao, Z.  
587 (2018) Phase stability and thermal equation of state of  $\delta$ -AlOOH: Implication for  
588 water transportation to the Deep Lower Mantle. *Earth and Planetary Science*  
589 *Letters*, 494, 92–98.

590 Dziewonski, A.M., and Anderson, D. L. (1981) Preliminary reference Earth model.  
591 *Physics of the Earth and Planetary Interiors*, 25, 297–356.

592 Fei, Y., Zhang, L., Corgne, A., Watson, H., Ricolleau, A., Meng, Y., and Prakapenka, V.  
593 (2007) Spin transition and equations of state of (Mg, Fe)O solid solutions.  
594 *Geophysical Research Letters*, 34, L17307.

595 Fukuyama, K., Ohtani, E., Shibazaki, Y., Kagi, H., and Suzuki, A. (2017) Stability field  
596 of phase Egg, AlSiO<sub>3</sub>OH at high pressure and high temperature: possible water  
597 reservoir in mantle transition zone. *Journal of Mineralogical and Petrological*  
598 *Sciences*, 112, 31–35.

599 Gasparik, T., Tripathi, A., and J.B. Parise. (2000) Structure of a new Al-rich phase, [K,  
600 Na]<sub>0.9</sub>[Mg, Fe]<sub>2</sub>[Mg, Fe, Al, Si]<sub>6</sub>O<sub>12</sub>, synthesized at 24 GPa. American  
601 Mineralogist, 85, 613–618.

602 Gleason, A.E., Quiroga, C.E., Suzuki, A., Pentcheva, R., and Mao, W.L. (2013)  
603 Symmetrization driven spin transition in  $\epsilon$ -FeOOH at high pressure. Earth and  
604 Planetary Science Letters, 379, 49–55.

605 Hsu, H. (2017) First-principles study of iron spin crossover in the new hexagonal  
606 aluminous phase. Physical Review B, 95, 020406.

607 Irifune, T. and Ringwood, A.E. (1993) Phase transformations in subducted oceanic crust  
608 and buoyancy relationships at depths of 600–800 km in the mantle. Earth and  
609 Planetary Science Letters, 117, 101–110.

610 Kagi, H., Ushijima, D., Sano-Furukawa, A., Komatsu, K., Iizuka, R., Nagai, T., and  
611 Nakano, S. (2010) Infrared absorption spectra of  $\delta$ -AlOOH and its deuteride at  
612 high pressure and implication to pressure response of the hydrogen bonds. Journal  
613 of Physics: Conference Series, 215, 012052.

614 Kaminsky, F.V. (2017) The Earth's Lower Mantle, Composition and Structure, 331 p.  
615 Springer International Publishing AG, Switzerland.

616 Kang, D., Feng, Y.-X., Yuan, Y., Ye, Q.-J., Zhu, F., Huo, H.-Y., Li, X.-Z., and Wu, X.  
617 (2017) Hydrogen-bond symmetrization of  $\delta$ -AlOOH. Chinese Physics Letters, 34,  
618 108301.

619 Kawazoe, T., Ohira, I., Ishii, T., Boffa Ballaran, T., McCammon, C., Suzuki, A., and  
620 Ohtani, E. (2017), Single crystal synthesis of  $\delta$ -(Al,Fe)OOH. American  
621 Mineralogist, 102, 1953–1956.

622 Kirby, S.H., Stein, S., Okal, E.A., and Rubie, D.C. (1996) Metastable mantle phase  
623 transformations and deep earthquakes in subducting oceanic lithosphere. *Reviews*  
624 *of Geophysics*, 34, 261–306.

625 Komatsu, K., Kuribayashi, T., Sano, A., Ohtani, E., and Kudoh, Y. (2006)  
626 Redetermination of the high-pressure modification of AlOOH from single-crystal  
627 synchrotron data. *Acta Crystallographica Section E*, 62, i216–218.

628 Kuribayashi, T., Sano-Furukawa, A., and Nagase, T. (2014) Observation of pressure-  
629 induced phase transition of  $\delta$ -AlOOH by using single-crystal synchrotron X-ray  
630 diffraction method. *Physics and Chemistry of Minerals*, 41, 303–312.

631 Li, S., Ahuja, R., and Johansson, B. (2006) The elastic and optical properties of the high-  
632 pressure hydrous phase  $\delta$ -AlOOH. *Solid State Communications*, 137, 101–106.

633 Lin, J.F., Shu, J., Mao, H.K., Hemley, R.J., and Shen, G. (2003) Amorphous boron gasket  
634 in diamond anvil cell research. *Review of Scientific Instruments*, 74, 4732–4736.

635 Lin, J.F., Struzhkin, V.V., Jacobsen, S.D., Hu, M.Y., Chow, P., Kung, J., Liu, H., Mao,  
636 H.-k., and Hemley, R. J. (2005) Spin transition of iron in magnesiowüstite in the  
637 Earth's lower mantle. *Nature*, 436, 377–380.

638 Liu, X., Matsukage, K.N., Nishihara, Y., Suzuki, T., and Takahashi, E. (2019) Stability of  
639 the hydrous phases of Al-rich Phase D and Al-rich Phase H in deep subducted  
640 oceanic crust. *American Mineralogist*, 104, 64–72.

641 Mao, Z., Lin, J.-F., Liu, J., and Prakapenka, V.B. (2011) Thermal equation of state of  
642 lower-mantle ferropicrinite across the spin crossover. *Geophysical Research*  
643 *Letters*, 38, L23308.

644 Mashino, I., Murakami, M., and Ohtani, E. (2016) Sound velocities of  $\delta$ -AlOOH up to  
645 core-mantle boundary pressures with implications for the seismic anomalies in the  
646 deep mantle. *Journal of Geophysical Research: Solid Earth*, 121, 595–609.

647 Masters, G., Laske, G., Bolton, H., and Dziewonski, A. (2000) The relative behavior of  
648 shear velocity, bulk sound speed, and compressional velocity in the mantle:  
649 Implications for chemical and thermal structure. In S.-I. Karato, A. Forte, R.  
650 Liebermann, G. Masters, and L. Stixrude, Eds., *Earth's deep interior: Mineral  
651 physics and tomography from the atomic to the global scale*, Geophysical  
652 Monograph 117, p. 63–87. the American Geophysical Union, U.S.A

653 Miura, H., Hamada, Y., Suzuki, T., Akaogi, M., Miyajima, N., and Fujino, K. (2000)  
654 Crystal structure of  $\text{CaMg}_2\text{Al}_6\text{O}_{12}$ , a new Al-rich high pressure form. *American  
655 Mineralogist*, 85, 1799–1803.

656 Miyajima, N., Yagi, T., Hirose, K., Kondo, T., Fujino, K., and Miura, H. (2001) Potential  
657 host phase of aluminum and potassium in the Earth's lower mantle. *American  
658 Mineralogist*, 86, 740–746.

659 Nishi, M., Irifune, T., Tsuchiya, J., Tange, Y., Nishihara, Y., Fujino, K., Higo, Y. (2014)  
660 Stability of hydrous silicate at high pressures and water transport to the deep  
661 lower mantle. *Nature Geoscience*, 7, 224–227.

662 Nishi, M., Irifune, T., Gréaux, S., Tange, Y., Higo, Y. (2015) Phase transitions of  
663 serpentine in the lower mantle. *Physics of the Earth and Planetary Interiors*, 245,  
664 52–58.

665 Nishi, M., Kuwayama, Y., Tsuchiya, J., and Tsuchiya, T. (2017) The pyrite-type high-  
666 pressure form of FeOOH. *Nature*, 547, 205–208.

667 Nishi, M., Tsuchiya, J., Arimoto, T., Kakizawa, S., Kunimoto, T., Tange, Y., Higo, Y.,  
668 Irifune, T. (2018) Thermal equation of state of  $\text{MgSiO}_4\text{H}_2$  phase H determined by  
669 in situ X-ray diffraction and a multianvil apparatus. *Physics and Chemistry of*  
670 *Minerals*, 45, 995–1001.

671 Nishihara, Y., and Matsukage, K.N. (2016) Iron-titanium oxyhydroxides as water carriers  
672 in the Earth's deep mantle. *American Mineralogist*, 101, 919–927.

673 Ohira, I., Ohtani, E., Sakai, T., Miyahara, M., Ohishi, Y., Hirao, N., and Nishijima, M.  
674 (2014) Stability of a hydrous  $\delta$ -phase,  $\text{AlOOH-MgSiO}_2(\text{OH})_2$ , and a mechanism  
675 for water transport into the base of lower mantle. *Earth and Planetary Science*  
676 *Letters*, 401, 12–17.

677 Ohishi, Y., Hirao, N., Sata, N., Hirose, K., and Takata, M. (2008) Highly intense  
678 monochromatic X-ray diffraction facility for high-pressure research at SPring-8.  
679 *High Pressure Research*, 28, 163–173.

680 Ohtani, E. (2005) Water in the mantle. *Elements*, 1, 25–30.

681 Ohtani, E. (2015) Hydrous minerals and the storage of water in the deep mantle.  
682 *Chemical Geology*, 418, 6–15.

683 Ohtani, E., Amaike, Y., Kamada, S., Ohira, I., and Mashino, I. (2016) Stability of  
684 hydrous minerals and water reservoirs in the deep Earth interior. In H. Terasaki,  
685 and R. A. Fischer, Eds., *Deep Earth: Physics and chemistry of the lower mantle*  
686 *and core*, Geophysical Monograph 217, p. 265–275. the American Geophysical  
687 Union, U.S.A.

688 Ohtani, E., Litasov, K., Suzuki, A., and Kondo, T. (2001) Stability field of new hydrous  
689 phase,  $\delta$ -AlOOH, with implications for water transport into the deep mantle.  
690 Geophysical Research Letters, 28, 3991–3994.

691 Okamoto, K., and Maruyama, S. (2004) The Eclogite–Garnetite transformation in the  
692 MORB + H<sub>2</sub>O system. Physics of the Earth and Planetary Interiors, 146, 283–296.

693 Otte, K., Pentcheva, R., Schmahl, W.W., and Rustad, J.R. (2009) Pressure-induced  
694 structural and electronic transitions in FeOOH from first principles. Physical  
695 Review B, 80, 205116.

696 Pamato, M.G., Myhill, R., Boffa Ballaran, T., Frost, D.J., Heidelbach, F., and Miyajima,  
697 N. (2015) Lower-mantle water reservoir implied by the extreme stability of a  
698 hydrous aluminosilicate. Nature Geoscience, 8, 75–79.

699 Panero, W.R., and Caracas, R. (2017) Stability of phase H in the MgSiO<sub>4</sub>H<sub>2</sub>–AlOOH–  
700 SiO<sub>2</sub> system. Earth and Planetary Science Letters, 463, 171–177.

701 Panero, W.R., and Stixrude, L.P. (2004) Hydrogen incorporation in stishovite at high  
702 pressure and symmetric hydrogen bonding in  $\delta$ -AlOOH. Earth and Planetary  
703 Science Letters, 221, 421–431.

704 Pearson, D.G., Brenker, F.E., Nestola, F., McNeill, J., Nasdala, L., Hutchison, M.T.,  
705 Matveev, S., Mather, K., Silversmit, G., Schmitz, S., Vekemans, B., and Vincze,  
706 L. (2014) Hydrous mantle transition zone indicated by ringwoodite included  
707 within diamond. Nature, 507, 221–224.

708 Pernet, M., Joubert, J.C., and Berthet-Colominas, C. (1975) Etude par diffraction  
709 neutronique de la forme haute pression de FeOOH. Solid State Communications,  
710 17, 1505–1510.



711 Pillai, S.B., Jha, P.K., Padmalal, A., Maurya, D.M., and Chamyal, L.S. (2018) First  
712 principles study of hydrogen bond symmetrization in  $\delta$ -AlOOH. Journal of  
713 Applied Physics, 123, 115901.

714 Ricard, Y., Mattern, E., and Matas, J. (2005) Synthetic tomographic images of slabs from  
715 mineral physics. In R. D. Van Der Hilst, J. D. Bass, J. Matas, and J. Trampert,  
716 Eds., Earth's Deep Mantle: Structure, Composition, and Evolution, Geophysical  
717 Monograph 160, p. 283–300. the American Geophysical Union, U.S.A

718 Sano, A., Ohtani, E., Kubo, T., and Funakoshi, K-i. (2004) In situ X-ray observation of  
719 decomposition of hydrous aluminosilicate  $\text{AlSiO}_3\text{OH}$  and aluminum oxide  
720 hydroxide  $\delta$ -AlOOH at high pressure and temperature. Journal of Physics and  
721 Chemistry of Solids, 65, 1547–1554.

722 Sano, A., Ohtani, E., Kondo, T., Hirao, N., Sakai, T., Sata, N., Ohishi, Y., and Kikegawa  
723 T. (2008) Aluminous hydrous mineral  $\delta$ -AlOOH as a carrier of hydrogen into the  
724 core-mantle boundary. Geophysical Research Letters, 35, L03303.

725 Sano-Furukawa, A., Komatsu, K., Vanpeteghem, C.B., and Ohtani, E. (2008) Neutron  
726 diffraction study of  $\delta$ -AlOOD at high pressure and its implication for  
727 symmetrization of the hydrogen bond. American Mineralogist, 93, 1558–1567.

728 Sano-Furukawa, A., Kagi, H., Nagai, T., Nakano, S., Fukura, S., Ushijima, D., Iizuka, R.,  
729 Ohtani, E., and Yagi, T. (2009) Change in compressibility of  $\delta$ -AlOOH and  $\delta$ -  
730 AlOOD at high pressure: A study of isotope effect and hydrogen-bond  
731 symmetrization. American Mineralogist, 94, 1255–1261.

732 Sano-Furukawa, A., Hattori, T., Komatsu, K., Kagi, H., Nagai, T., Molaison, J.J., dos  
733 Santos, A.M., and Tulk, C.A. (2018) Direct observation of symmetrization of

734 hydrogen bond in  $\delta$ -AlOOH under mantle conditions using neutron diffraction.  
735 Scientific Reports, 8, 15520.

736 Seto, Y., Nishio-Hamane, D., Nagai, T., and Sata, N. (2010) Development of a software  
737 suite on X-ray diffraction experiments. The Review of High Pressure Science and  
738 Technology, 20, 269–276 (in Japanese).

739 Smyth, J.R., and Jacobsen, S.D. (2006) Nominally anhydrous minerals and Earth's deep  
740 water cycle. In S.D. Jacobsen, and S. van der Lee Eds., Earth's Deep Water Cycle,  
741 Geophysical Monograph Series 168, p. 1–11. the American Geophysical Union,  
742 U.S.A

743 Solomatova, N.V., Jackson, J.M., Sturhahn, W., Wicks, J.K., Zhao, J., Toellner, T.S.,  
744 Kalkan, B., and Steinhardt, W.M. (2016) Equation of state and spin crossover of  
745 (Mg,Fe)O at high pressure, with implications for explaining topographic relief at  
746 the core-mantle boundary. American Mineralogist, 101, 1084–1093.

747 Solomatova, N.V., Jackson, J.M., Sturhahn, W., Rossman, G.R., and Roskosz, M. (2017)  
748 Electronic environments of ferrous iron in rhyolitic and basaltic glasses at high  
749 pressure. Journal of Geophysical Research: Solid Earth, 122, 6306–6322.

750 Sturhahn, W. (2000) CONUSS and PHOENIX: Evaluation of nuclear resonant scattering  
751 data. Hyperfine Interactions, 125, 149–172.

752 ——— (2016) CONUSS (COherent NUclear resonant Scattering by Single crystals).  
753 Open source software, <http://www.nrixs.com>.

754 ——— (2018) MINUTI (MINeral physics UTILities). Open source software,  
755 <http://www.nrixs.com>.

756 Suzuki, A. (2009) Compressibility of the high-pressure polymorph of AlOOH to 17 GPa.  
757 Mineralogical Magazine, 73, 479–485.

758 ——— (2010) High-pressure X-ray diffraction study of  $\epsilon$ -FeOOH. Physics and  
759 Chemistry of Minerals, 37, 153–157

760 ——— (2016) Pressure–volume–temperature equation of state of  $\epsilon$ -FeOOH to 11 GPa  
761 and 700 K. Journal of Mineralogical and petrological Science, 111, 420–424.

762 Suzuki, A., Ohtani, E., and Kamada, T. (2000) A new hydrous phase  $\delta$ -AlOOH  
763 synthesized at 21 GPa and 1000 °C. Physics and Chemistry of Minerals, 27, 689–  
764 693.

765 Tackley, P.J. (2011) Living dead slabs in 3-D: The dynamics of compositionally-  
766 stratified slabs entering a “slab graveyard” above the core-mantle boundary.  
767 Physics of the Earth and Planetary Interiors, 188, 150–162.

768 Takemura, K., Sahu, P.Ch., Kunii, Y., and Toma, Y. (2001) Versatile gas-loading system  
769 for diamond-anvil cells. Review of Scientific Instruments, 72, 3873–3876.

770 Thompson E.C., Campbell, A. J., and Tsuchiya, J. (2017) Elasticity of  $\epsilon$ -FeOOH: Seismic  
771 implications for Earth’s lower mantle. Journal of Geophysical Research: Solid  
772 Earth, 122, 5038–5047.

773 Toellner, T.S. (2000) Monochromatization of synchrotron radiation for nuclear resonant  
774 scattering experiments. Hyperfine Interactions, 125, 3–28.

775 Trampert, J., Deschamps, F., Resovsky, J., and Yuen, D. (2004) Probabilistic tomography  
776 maps chemical heterogeneities throughout the lower mantle. Science, 306, 853–  
777 856.

778 Tschauner, O., Huang, S., Greenberg, E., Prakapenka, V.B., Ma, C., Rossman, G.R.,  
779 Shen, A.H., Zhang, D., Newville, M., Lanzirotti, A., and Tait, K. (2018) Ice-VII  
780 inclusions in diamonds: Evidence for aqueous fluid in Earth's deep mantle.  
781 *Science*, 359, 1136–1139.

782 Tsuchiya, J. and Mookherjee, M. (2015) Crystal structure, equation of state, and  
783 elasticity of phase H ( $\text{MgSiO}_4\text{H}_2$ ) at Earth's lower mantle pressures. *Scientific*  
784 *Reports*, 5, 15534.

785 Tsuchiya, J. and Tsuchiya, T. (2009) Elastic properties of  $\delta$ -AlOOH under pressure: First  
786 principles investigation. *Physics of the Earth and Planetary Interiors*, 174, 122–  
787 127.

788 Tsuchiya, J., Tsuchiya, T., Tsuneyuki, S., and Yamanaka T. (2002), First principles  
789 calculation of a high-pressure hydrous phase,  $\delta$ -AlOOH. *Geophysical Research*  
790 *Letters*, 29, 1909.

791 van der Meer, D.G., Spakman, W., van Hinsbergen, D.J.J., Amaru, M.L., Torsvik, T.H.  
792 (2010) Towards absolute plate motions constrained by lower-mantle slab  
793 remnants. *Nature Geoscience*, 3, 36–40.

794 Vanpeteghem, C.B., Ohtani, E., and Kondo, T. (2002) Equation of state of the hydrous  
795 phase  $\delta$ -AlOOH at room temperature up to 22.5 GPa. *Geophysical Research*  
796 *Letters*, 29, 1119.

797 Walter, M.J., Thomson, A.R., Wang, W., Lord, O.T., Ross, J., McMahon, S.C., Baron,  
798 M.A., Melekhova, E., Kleppe, A.K., and Kohn, S.C. (2015) The stability of  
799 hydrous silicates in Earth's lower mantle: experimental constraints from the

800 systems MgO–SiO<sub>2</sub>–H<sub>2</sub>O and MgO–Al<sub>2</sub>O<sub>3</sub>–SiO<sub>2</sub>–H<sub>2</sub>O. *Chemical Geology*, 418,  
801 16–29.

802 Wirth, R., Vollmer, C., Brenker, F., Matsyuk, S., and Kaminsky, F. (2007) Inclusions of  
803 nanocrystalline hydrous aluminium silicate “Phase Egg” in superdeep diamonds  
804 from Juina (Mato Grosso State, Brazil). *Earth and Planetary Science Letters*, 259,  
805 384–399.

806 Wu, Y., Wu, X., Lin, L.-F., McCammon, C.A., Xiao, Y., Chow, P., Prakapenka, V.B.,  
807 Yoshino, T., Zhai, S., and Qin, S. (2016) Spin transition of ferric iron in the NAL  
808 phase: Implications for the seismic heterogeneities of subducted slabs in the lower  
809 mantle. *Earth and Planetary Science Letters*, 434, 91–100.

810 Xue, X., and Kanzaki, M. (2007) High-pressure  $\delta$ -Al(OH)<sub>3</sub> and  $\delta$ -AlOOH phases and  
811 isostructural hydroxides/oxyhydroxides: New structural insights from high-  
812 resolution <sup>1</sup>H and <sup>27</sup>Al NMR. *The Journal of physical Chemistry B*, 111, 13156–  
813 13166.

814

815

### FIGURE CAPTIONS

816 **Figure 1.** One dimensional XRD patterns of  $\delta$ -Fe12 (Run# DAF01) acquired at 12.3 and  
817 44.0 GPa. The patterns were obtained during compression. Legend:  $\delta$ ,  $\delta$ -phase ( $\delta$ -Fe12);  
818 He, solid helium (pressure medium); Re, rhenium (gasket material).  $\lambda$  indicates the  
819 wavelength of the X-rays. The uncertainty of  $\lambda$  is given in parenthesis for the last reported  
820 significant digit.

821

822 **Figure 2.** *P-V* profiles of  $\delta$ -(Al,Fe)OOH ( $\delta$ -Fe12,  $\delta$ -Fe5, Fe-free  $\delta$ -AlOOH). Blue circles  
823 and light blue diamonds indicate the data of  $\delta$ -Fe12 and  $\delta$ -Fe5, respectively.  
824 Experimental data for Fe-free  $\delta$ -AlOOH are cited from Sano-Furukawa et al. (2009) (Red  
825 squares, S09) and Kuribayashi et al. (2014) (purple triangles, K14). Solid and open  
826 symbols indicate the data acquired during compression and decompression, respectively.  
827 The uncertainties of pressure and volume are smaller than the symbols. In the case of the  
828 data of Fe-free  $\delta$ -AlOOH, only the data obtained in which helium was used as the  
829 pressure medium were selected.

830

831 **Figure 3.** Axial ratios (left figures) and normalized lattice constants (right figures) as a  
832 function of pressure for  $\delta$ -(Al,Fe)OOH ( $\delta$ -Fe12,  $\delta$ -Fe5, Fe-free  $\delta$ -AlOOH). Blue circles  
833 and light blue diamonds indicate the data of  $\delta$ -Fe12 and  $\delta$ -Fe5, respectively. The  
834 experimental data for Fe-free  $\delta$ -AlOOH are cited from Sano-Furukawa et al. (2009) (Red  
835 squares, S09) and Kuribayashi et al. (2014) (purple triangles, K14). In the case of the data  
836 of Fe-free  $\delta$ -AlOOH, only the data obtained in which helium was used as the pressure  
837 medium were selected. To calculate the normalized lattice constants of  $\delta$ -Fe12 and  $\delta$ -Fe5,  
838 the ambient pressure lattice constants of a  $\delta$ -(Al<sub>0.807(7)</sub><sup>57</sup>Fe<sub>0.117(4)</sub>)OOH<sub>1.15(3)</sub> sample (the  
839 CIF file is in the deposit), having an identical Fe/(Al+Fe) ratio to the  $\delta$ -Fe12 sample  
840 within error, were used for  $\delta$ -Fe12 data ( $a_0 = 4.7458(13)$  Å,  $b_0 = 4.2564(11)$  Å,  $c_0 =$   
841  $2.8519(6)$  Å), and those of  $\delta$ -Fe5 which were measured at BL10XU after decompression  
842 were used for  $\delta$ -Fe5 data ( $a_0 = 4.7266(7)$  Å,  $b_0 = 4.2389(10)$  Å,  $c_0 = 2.8401(3)$  Å).

843

844 **Figure 4.** The  $f$ - $F$  plots of  $\delta$ -(Al,Fe)OOH ( $\delta$ -Fe12,  $\delta$ -Fe5, Fe-free  $\delta$ -AlOOH) based on  
845 data from this study, Sano-Furukawa et al. (2009) (S09), and Kuribayashi et al. (2014)  
846 (K14). For  $\delta$ -Fe12 and  $\delta$ -Fe5, the  $V_0$  obtained from 2nd BM EoS fits for the  $P2_1nm$   
847 structures were used in their plots (Table 3). The decrease or constant value in  $F$  between  
848  $f = 0$  and  $\sim 0.02$  are observed in all the data. The kink at  $\sim 10$  GPa ( $f = \sim 0.02$ ) in the  $f$ - $F$   
849 plots corresponds to the change in axial compressibility, suggesting that the  $\delta$ -  
850 (Al,Fe)OOH phases could be classified into two structures with different compressibility  
851 with boundary of 10 GPa. The decrease in  $F$  between 32 and 40 GPa ( $f = \sim 0.05$ – $0.06$ ) is  
852 seen only in the data for the Fe-bearing  $\delta$ -phases, which results from the spin transition of  
853  $\text{Fe}^{3+}$ .

854

855 **Figure 5.**  $P$ - $V$  profiles with the fitted spin crossover EoS for  $\delta$ -Fe12 (blue circles with a  
856 gray line) and  $\delta$ -Fe5 (light blue diamonds with a light gray line). The lines are spin  
857 crossover EoS fitted with the MINUTI software (Sturhahn 2018). The inset indicates the  
858 normalized residuals of fitting with  $1\sigma$  error bars. The uncertainties of pressure and  
859 volume are smaller than the symbols, and those of the spin transition pressure values are  
860 given in parentheses for the last reported significant digit.

861

862 **Figure 6.** Isothermal bulk modulus ( $K_T$ ), density ( $\rho$ ), bulk sound velocity ( $v_\Phi$ ), the ratio of  
863  $\rho$  and  $v_\Phi$ , and their uncertainties as a function of pressure for  $\delta$ -Fe12 and  $\delta$ -Fe5, resulting  
864 from the spin crossover EoS fitted with MINUTI software (Sturhahn 2018). The EoS  
865 parameters and fitting curves are shown in Table 3 and Fig. 5, respectively. The error for  
866 each parameter is indicated by the gray area.

867

868 **Figure 7.** Synchrotron Mössbauer spectra of  $\delta$ -Fe13 at six pressure conditions, without  
869 the stainless steel reference foil (blue) and with the stainless steel (SS) foil (orange) in the  
870 X-ray beam path, and their corresponding best fits (solid lines). The fitted hyperfine  
871 parameters are given in Table 4. The reduced  $\chi^2$  for each dual fit is shown in the lower  
872 left corner. The uncertainties of pressure are given in parentheses for the last reported  
873 significant digit.

874

875 **Figure 8.** Quadrupole splitting and isomer shift (relative to  $\alpha$ -Fe) of  $\delta$ -Fe13. Orange  
876 squares correspond to a high-spin  $\text{Fe}^{3+}$ -like site, dark blue circles are a low-spin  $\text{Fe}^{3+}_A$  site  
877 with a low quadrupole splitting, and light blue diamonds are a low-spin  $\text{Fe}^{3+}_B$  site with an  
878 intermediate quadrupole splitting. See Table 4 for tabulated hyperfine parameters.

879

880 **Figure 9.** (a) Isothermal bulk modulus, (b) density, (c) bulk sound velocity, and (d) the  
881 ratio of density and bulk sound velocity as a function of pressure for  $\delta$ -Fe12 (blue solid  
882 line),  $\delta$ -Fe5 (light blue solid line),  $\delta$ -AlOOH (red dash-dot line),  $\text{MgSiO}_4\text{H}_2$  Phase H  
883 (green dash-dot line),  $\epsilon$ -FeOOH (brown dotted line), and Fe-bearing NAL phase having a  
884 chemical composition of  $\text{Na}_{0.71}\text{Mg}_{2.05}\text{Al}_{4.62}\text{Si}_{1.16}\text{Fe}^{2+}_{0.09}\text{Fe}^{3+}_{0.17}\text{O}_{12}$  (orange dash-dot line).  
885 PREM (Dziewonski and Anderson 1981) values are also shown for reference in (b)–(d)  
886 (black dash line). The red dash-dot lines for  $\delta$ -AlOOH with  $Pnmm$  structure are obtained  
887 from the 3rd-order BM EoS fitting with MINUTI software (Sturhahn 2018), using the  
888 pressure-volume dataset at the room temperature and pressures higher than 20 GPa  
889 reported in both Sano-Furukawa et al. (2009) and Duan et al. (2018). The green dash-dot



890 lines for Phase H and the brown dotted lines for  $\epsilon$ -FeOOH are reproduced with the 2nd or  
891 3rd EoS parameters reported in Nishi et al. (2018) and Thompson et al. (2017),  
892 respectively. The orange dash-dot lines indicate the data of Fe-bearing NAL phase, which  
893 are determined by re-fitting for the  $P$ - $V$  data of this phase (Wu et al. 2016) using MINUTI  
894 software to obtain fit parameter error correlations and a consistency in the comparison of  
895 trends. Solid and dash-dot lines are based on the experimental data at 300 K reported in  
896 this study and the previous studies, while the dotted lines are based on theory at 0 K. The  
897 errors for the data of  $\delta$ -Fe12 and  $\delta$ -Fe5 are only shown in Figure 6 to prevent the error  
898 bars from overlapping with the other lines in this figure.

899

900 **Table 1.** Lattice constants and unit cell volumes determined for  $\delta$ -Fe12,  $\delta$ -

901  $(\text{Al}_{0.832(5)}^{57}\text{Fe}_{0.117(1)})\text{OOH}_{1.15(3)}$  ( $\text{Fe}/(\text{Al}+\text{Fe}) = 0.123(2)$ ).

$P_w$ (GPa)	$P_{\text{ruby}}$ (GPa)	$a$ (Å)	$b$ (Å)	$c$ (Å)	$V$ (Å <sup>3</sup> )
<i>Compression</i>					
1.07(1)		4.7401(4)	4.2488(8)	2.8522(2)	57.44(3)
2.01(5)	1.62(8)	4.7301(3)	4.2376(5)	2.8486(1)	57.10(2)
4.65(3)	4.18(11)	4.7048(4)	4.2062(6)	2.8379(2)	56.16(2)
6.00(2)	5.54(15)	4.6919(3)	4.1920(5)	2.8321(2)	55.70(2)
7.71(5)		4.6781(4)	4.1725(5)	2.8256(2)	55.15(3)
7.83(2)		4.6762(5)	4.1711(6)	2.8248(2)	55.10(3)
10.13(6)	9.49(25)	4.6591(2)	4.1520(4)	2.8154(1)	54.46(2)
12.29(11)	11.86(1)	4.6456(4)	4.1403(6)	2.8075(2)	54.00(3)
17.38(5)	16.57(33)	4.6148(2)	4.1147(3)	2.7884(1)	52.95(1)
20.96(6)		4.5951(4)	4.0971(7)	2.7753(2)	52.24(3)
24.47(4)	23.76(30)	4.5763(2)	4.0832(3)	2.7637(1)	51.64(1)
28.62(3)	27.79(29)	4.5565(2)	4.0662(4)	2.7503(1)	50.96(2)
32.67(9)	31.73(22)	4.5373(4)	4.0532(8)	2.7379(3)	50.35(3)
37.93(15)		4.4967(5)	4.0170(8)	2.7104(3)	48.96(3)
40.83(49)		4.4840(6)	4.0065(7)	2.7002(3)	48.51(3)
44.03(58)		4.4703(7)	3.9936(9)	2.6901(4)	48.02(4)
46.88(45)		4.4602(9)	3.9852(18)	2.6829(4)	47.69(7)
50.85(33)		4.4455(10)	3.9750(20)	2.6742(5)	47.26(8)

53.80(35)	4.4351(17)	3.9663(25)	2.6678(7)	46.93(11)
58.27(34)	4.4205(15)	3.9536(22)	2.6568(6)	46.43(9)
62.04(33)	4.4094(9)	3.9434(13)	2.6500(3)	46.08(5)
64.83(35)	4.4009(15)	3.9394(18)	2.6427(6)	45.82(8)

Decompression

53.97(6)	4.4405(11)	3.9684(15)	2.6704(6)	47.06(7)
47.17(7)	4.4607(6)	3.9851(8)	2.6845(4)	47.72(4)
44.23(11)	4.4707(6)	3.9940(7)	2.6913(4)	48.06(4)
42.06(20)	4.4799(5)	4.0018(8)	2.6974(3)	48.36(3)
37.02(26)	4.5046(3)	4.0255(5)	2.7156(2)	49.24(2)
35.22(28)	4.5222(5)	4.0397(7)	2.7267(2)	49.81(3)
33.16(26)	4.5328(6)	4.0492(9)	2.7334(3)	50.17(4)
32.14(10)	4.5444(6)	4.0556(12)	2.7398(4)	50.50(5)
29.79(5)	4.5586(4)	4.0660(7)	2.7498(2)	50.97(3)

902

903  $P_W$  and  $P_{\text{ruby}}$  indicate the pressure values determined using the EoS for tungsten  
904 (Dorogokupets and Oganov 2006) which are used as the experimental pressure, and the  
905 ruby fluorescence method (Dewaele et al. 2008), respectively. Uncertainties are given in  
906 parentheses for the last reported significant digit.

907

908

909

910

911

912

913

914

915

916

917

918  
 919  
 920  
 921  
 922  
 923  
 924  
 925  
 926  
 927

928 **Table 2.** Lattice constants and unit cell volumes determined for  $\delta$ -Fe5 ( $\delta$ -  
 929  $(\text{Al}_{0.908(9)}^{57}\text{Fe}_{0.045(1)})\text{OOH}_{1.14(3)}$  ( $\text{Fe}/(\text{Al}+\text{Fe}) = 0.047(10)$ ).

$P_{\text{W}}$ (GPa)	$P_{\text{ruby}}$ (GPa)	$a$ (Å)	$b$ (Å)	$c$ (Å)	$V$ (Å <sup>3</sup> )
<i>Compression</i>					
2.04(4)		4.7105(3)	4.2200(5)	2.8343(2)	56.34(2)
3.44(14)		4.6946(2)	4.2021(3)	2.8279(1)	55.79(1)
5.50(11)		4.6778(2)	4.1816(4)	2.8207(1)	55.17(2)
8.36(11)	7.73(14)	4.6515(3)	4.1490(4)	2.8091(1)	54.21(2)
12.36(18)		4.6244(2)	4.1244(3)	2.7934(1)	53.28(1)
13.67(30)	12.96(6)	4.6163(2)	4.1171(3)	2.7883(1)	52.99(2)
18.57(11)		4.5873(1)	4.0932(1)	2.7702(0)	52.02(1)
20.82(31)		4.5758(2)	4.0838(3)	2.7628(1)	51.63(1)
22.76(17)		4.5647(3)	4.0751(5)	2.7558(2)	51.26(2)
24.35(25)		4.557(2)	4.0698(4)	2.7511(1)	51.03(2)
25.63(56)	25.68(32)	4.5487(2)	4.0615(4)	2.7458(1)	50.73(2)
34.99(22)		4.5044(4)	4.0248(6)	2.7173(2)	49.26(3)
35.46(9)		4.5030(5)	4.0243(8)	2.7161(3)	49.22(3)
35.80(23)		4.4987(4)	4.0207(7)	2.7135(2)	49.08(3)
37.10(10)		4.4919(4)	4.0149(7)	2.7089(2)	48.85(3)
37.62(34)		4.4893(5)	4.0116(7)	2.7065(2)	48.74(3)
39.51(29)		4.4799(6)	4.0048(9)	2.7003(3)	48.45(4)
40.34(29)		4.4767(6)	4.0016(10)	2.6982(3)	48.34(4)

42.68(63)	4.4680(5)	3.9945(6)	2.6925(2)	48.05(3)
45.91(37)	4.4548(8)	3.9844(12)	2.6839(4)	47.64(5)
49.31(38)	4.4423(9)	3.9747(17)	2.6748(4)	47.23(7)
52.52(17)	4.4296(11)	3.9670(16)	2.6673(4)	46.87(7)
55.60(16)	4.4211(9)	3.9555(18)	2.6601(4)	46.52(7)
<u>Decompression</u>				
38.27(41)	4.4863(5)	4.0095(6)	2.7025(3)	48.61(3)
36.98(14)	4.4910(7)	4.0150(8)	2.7061(4)	48.80(4)
36.06(15)	4.4994(5)	4.0203(8)	2.7120(6)	49.06(4)
35.23(13)	4.5028(4)	4.0229(7)	2.7140(3)	49.16(3)
34.13(12)	4.5117(6)	4.0293(10)	2.7187(4)	49.42(4)
31.65(7)	4.5228(4)	4.0398(6)	2.7266(2)	49.82(3)
29.08(23)	4.5339(2)	4.0510(3)	2.7361(1)	50.25(2)
0.0001	4.7266(7)	4.2389(10)	2.8401(3)	56.90(5)

930

931  $P_W$  and  $P_{\text{ruby}}$  indicate the pressure values determined using the EoS for tungsten  
932 (Dorogokupets and Oganov 2006) which are used as the experimental pressure, and the  
933 ruby fluorescence method (Dewaele et al. 2008), respectively. Uncertainties are given in  
934 parentheses for the last reported significant digit.

935

936

937

938

939

940

941

942

943

944

945

946

947

948

949

950

951

952

953

954

955

956 **Table 3.** EoS Parameters of  $\delta$ -(Al,Fe)OOH phases.

Phase	$V_0$ ( $\text{\AA}^3$ )	$K_0$ (GPa)	$K'$ (GPa)	EoS	$P$ range	Details
<u>This study</u>						
$\delta$ -(Al <sub>0.832(5)</sub> <sup>57</sup> Fe <sub>0.117(1)</sub> )OOH <sub>1.15(3)</sub>	57.85(2)	147(1)	4 (fixed)	2nd BM	1.0–10.1 GPa	$\delta$ -Fe12 (Fe/(Al+Fe) = 0.123(2)), $P2_1nm$ , HS
$\delta$ -(Al <sub>0.832(5)</sub> <sup>57</sup> Fe <sub>0.117(1)</sub> )OOH <sub>1.15(3)</sub>	57.5(3)	155(22)	8(2)	Spin crossover EoS	10.1–64.8 GPa	$\delta$ -Fe12 (Fe/(Al+Fe) = 0.123(2)), $Pnmm$ , HS
$\delta$ -(Al <sub>0.832(5)</sub> <sup>57</sup> Fe <sub>0.117(1)</sub> )OOH <sub>1.15(3)</sub>	55.2(4)	241(14)	4 (fixed)	Spin crossover EoS		$\delta$ -Fe12 (Fe/(Al+Fe) = 0.123(2)), $Pnmm$ , LS
$\delta$ -(Al <sub>0.908(9)</sub> <sup>57</sup> Fe <sub>0.045(1)</sub> )OOH <sub>1.14(3)</sub>	57.03(7)	152(7)	4 (fixed)	2nd BM	0–8.4 GPa	$\delta$ -Fe5 (Fe/(Al+Fe) = 0.047(10)), $P2_1nm$ , HS
$\delta$ -(Al <sub>0.908(9)</sub> <sup>57</sup> Fe <sub>0.045(1)</sub> )OOH <sub>1.14(3)</sub>	56.9(4)	149(25)	8(2)	Spin crossover EoS	12.4–55.6 GPa	$\delta$ -Fe5 (Fe/(Al+Fe) = 0.047(10)), $Pnmm$ , HS
$\delta$ -(Al <sub>0.908(9)</sub> <sup>57</sup> Fe <sub>0.045(1)</sub> )OOH <sub>1.14(3)</sub>	55.4(3)	223(11)	4 (fixed)	Spin crossover EoS		$\delta$ -Fe5 (Fe/(Al+Fe) = 0.047(10)), $Pnmm$ , LS
<u>Previous study</u>						References
$\delta$ -AlOOH	56.408(9)	152(2)	4 (fixed)	2nd BM	0–10 GPa	Sano-Furukawa et al. (2009)
$\delta$ -AlOOH	55.47(8)	219(3)	4 (fixed)	2nd BM	10–63.5 GPa	Sano-Furukawa et al. (2009)
$\delta$ -AlOOH	56.408(9)	191(1)	4 (fixed)	2nd BM	0–63.5 GPa	Sano-Furukawa et al. (2009)
$\delta$ -AlOOH	56.408(9)	162(3)	5.9(2)	3rd BM	0–63.5 GPa	Sano-Furukawa et al. (2009)
$\delta$ -AlOOH	56.54(9)	252(3)	4 (fixed)	3rd BM	0–22.5 GPa	Vanpeteghem et al. (2002)
$\delta$ -AlOOH	56.35(2)	124(2)	13.5(7)	3rd BM	0–17.1 GPa	Suzuki (2009)
$\delta$ -AlOOH <sup>a</sup>	167	167	5.0	Vinet	0–28 GPa	Tsuchiya and Tsuchiya (2009)
$\delta$ -AlOOH <sup>b</sup>	57.57	205	4.3	Vinet	0–150 GPa	Tsuchiya and Tsuchiya (2009)
$\epsilon$ -FeOOH <sup>c</sup>	66.3(5)	158(5)	4 (fixed)	2nd BM	0–21 GPa	Gleason et al. (2008)
$\epsilon$ -FeOOH	66.20(3)	126(3)	10(1)	3rd BM	0–8.6 GPa	Suzuki (2010)
$\epsilon$ -FeOOH	66.278(6)	135(3)	6.1(9)	3rd BM	0–11.1 GPa	Suzuki (2016)

957

958 Uncertainties are given in parentheses for the last reported significant digit.

959 HS, high-spin state; LS, low-spin state

960 a, Theory,  $P2_1nm$  structure.961 b, Theory,  $Pnmm$  (HC) structure.

962 c, Experimental data were obtained at 473–673 K.

963 d, Theory,  $Pnmm$  (HC) structure and low-spin state.

964

965

966 **Table 4.** Hyperfine parameters for  $\delta$ -Fe13 and the corresponding reduced  $\chi^2$  produced  
 967 from fitting the spectra of the sample with and without the stainless steel reference foil  
 968 simultaneously. Uncertainties are given in parentheses for the last reported significant  
 969 digit. Isomer shifts are relative to  $\alpha$ -Fe metal. In low-spin  $\delta$ -Fe13,  $\text{Fe}^{3+}_{\text{B}}/(\text{Fe}^{3+}_{\text{A}} + \text{Fe}^{3+}_{\text{B}})$   
 970 was found to be 1/3 through Monte-Carlo searches and did not change with pressure, and  
 971 so was fixed to reduce parameter correlations. See text for more details.

<u>HS</u>					
Pressure (GPa)	QS (mm/s)	IS (mm/s)	FWHM (mm/s)	Thickness ( $\mu\text{m}$ )	reduced $\chi^2$
21.1(2)	0.414(7)	0.19(2)	0.12(1)	23.8(5)	1.36(6)
31.8(8)	0.392(3)	0.18(2)	0.01(5)	26.4(2)	1.88(7)

<u>LS</u>								
Pressure (GPa)	QS <sub>A</sub> (mm/s)	IS <sub>A</sub> (mm/s)	FWHM <sub>A</sub> (mm/s)	QS <sub>B</sub> (mm/s)	IS <sub>B</sub> (mm/s)	FWHM <sub>B</sub> (mm/s)	Thickness ( $\mu\text{m}$ )	reduced $\chi^2$
45(2)	1.140(4)	0.209(7)	0.260(4)	1.73(1)	0.249(7)	0.16(1)	19.8(5)	1.23(5)
59(2)	1.235(6)	0.135(8)	0.221(5)	1.864(7)	0.206(9)	0.22(1)	18.0(4)	1.12(5)
67.5(5)	1.291(6)	0.107(6)	0.215(4)	1.88(1)	0.172(9)	0.28(2)	16.9(2)	1.50(6)
78.5(5)	1.320(6)	0.109(7)	0.227(4)	2.006(9)	0.202(9)	0.28(2)	16.1(2)	1.61(6)

972

973

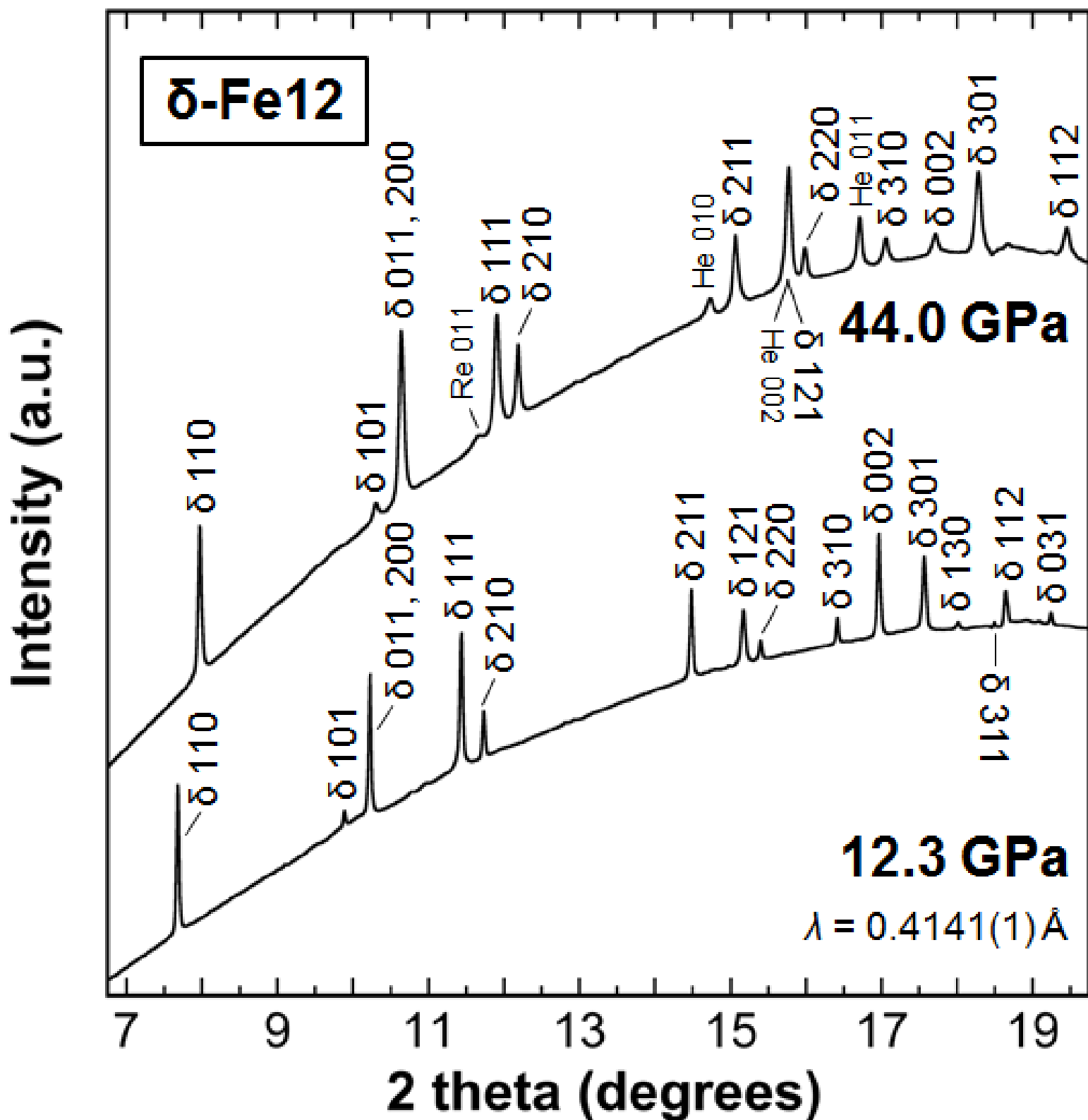
974 **Table 5.** Euler angles  $\alpha$  and  $\beta$  for the electric field gradient orientation of high-spin (HS)  
975 and low-spin (LS) ferric iron sites in  $\delta$ -Fe13.

	$\alpha$	$\beta$
HS Fe <sup>3+</sup>	0°	0°
LS Fe <sup>3+</sup> <sub>A</sub>	296°	261°
LS Fe <sup>3+</sup> <sub>B</sub>	22°	253°

976

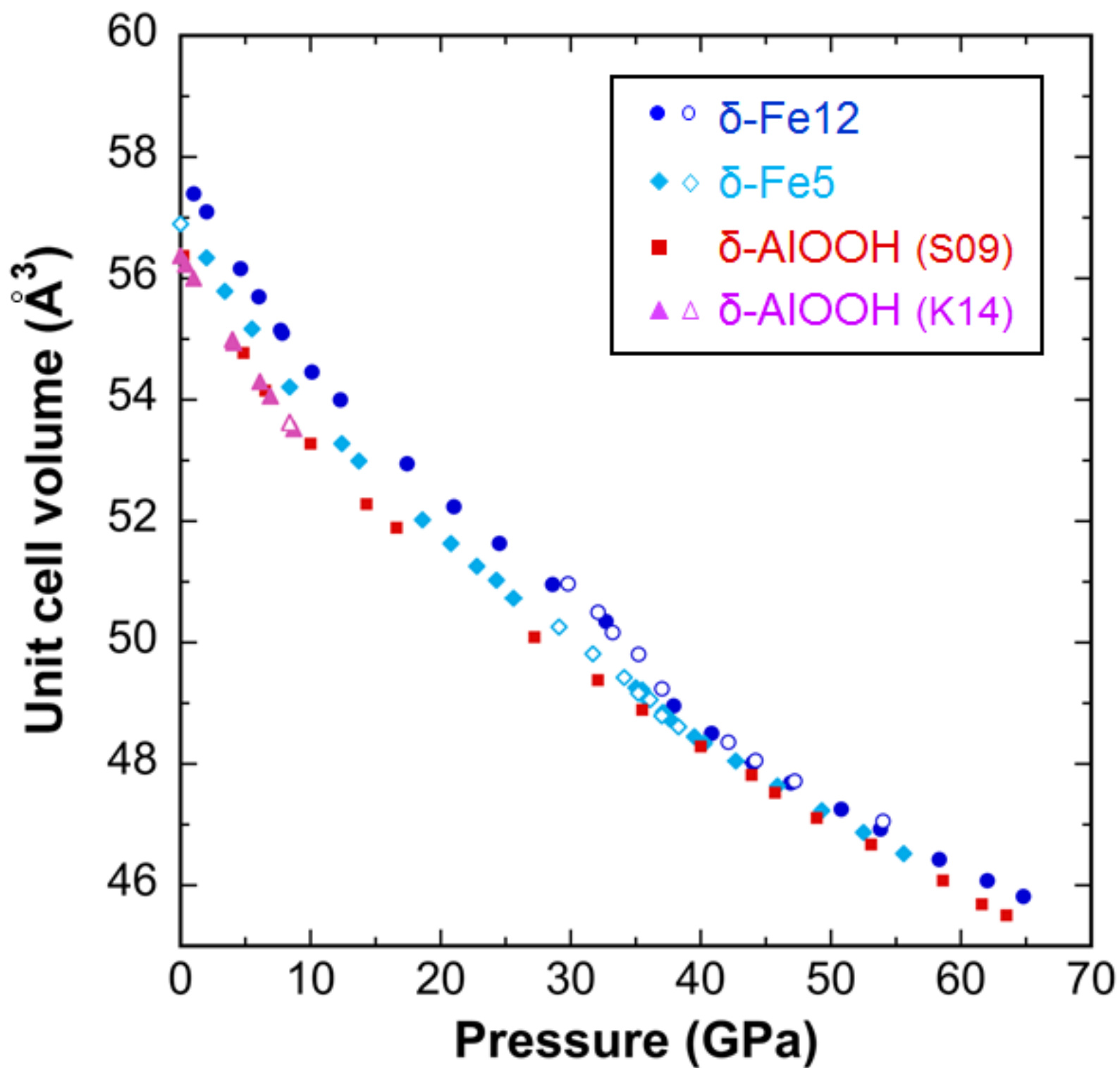
977

Figure 1





**Figure 2**



**Figure 3**

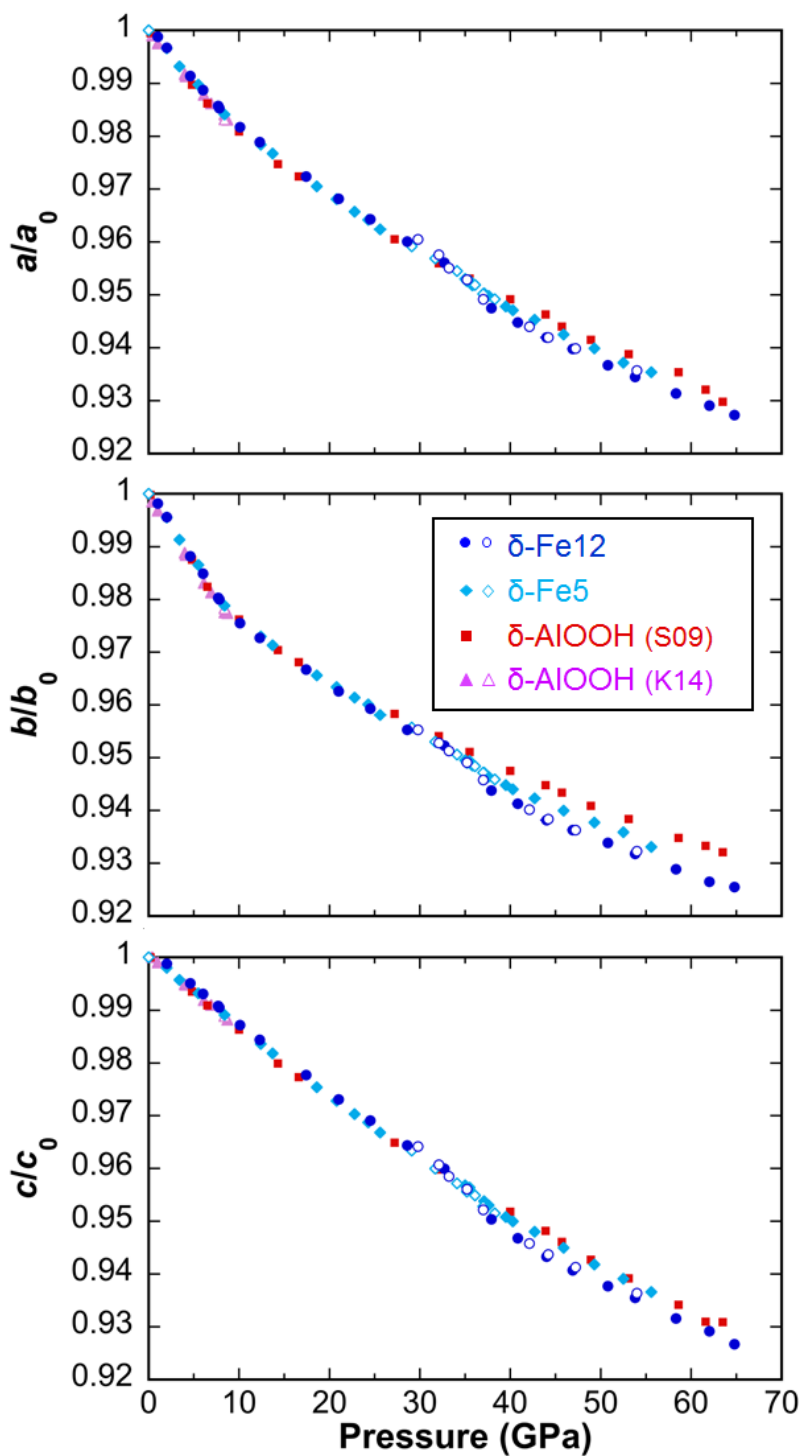
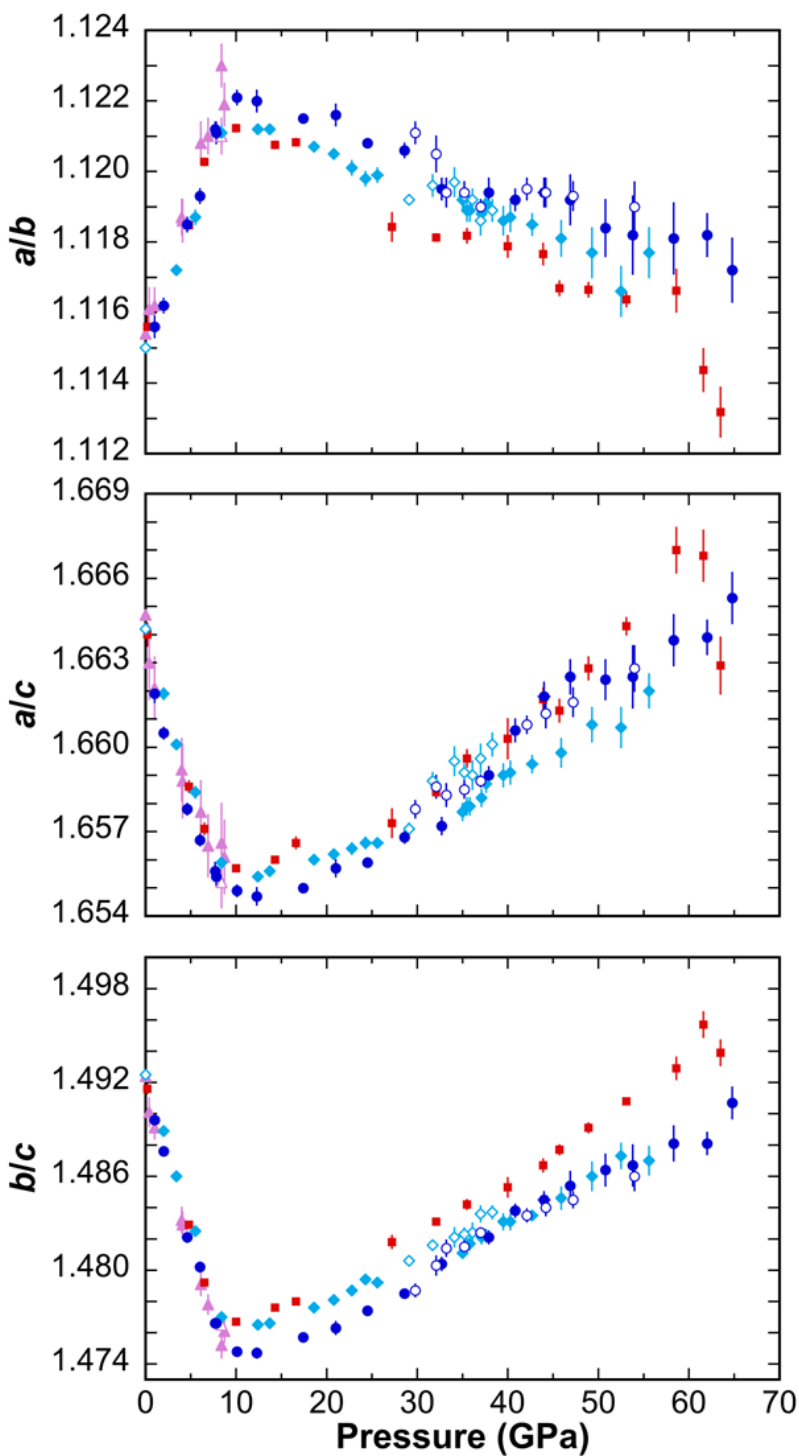


**Figure 4**

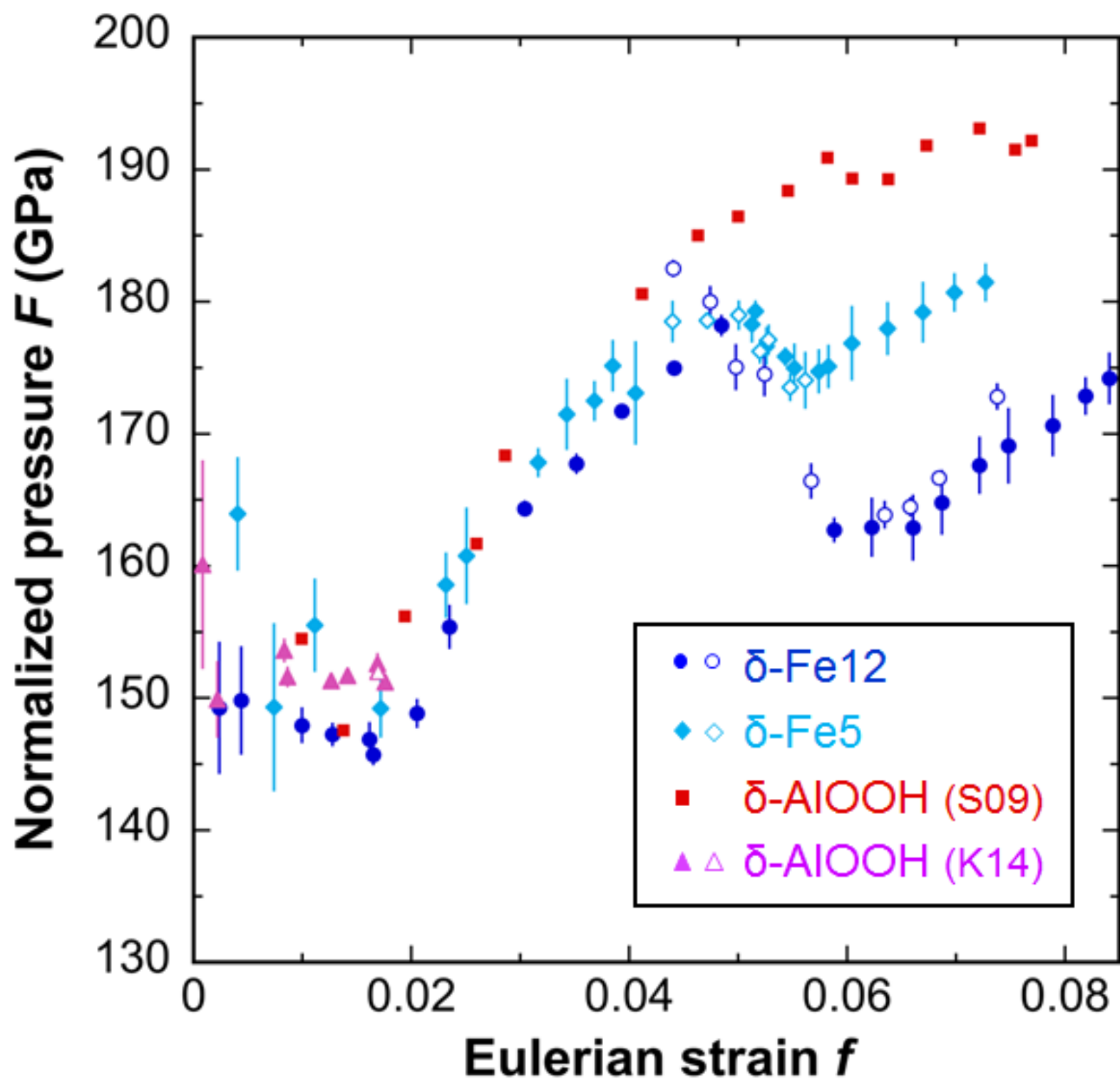


Figure 5

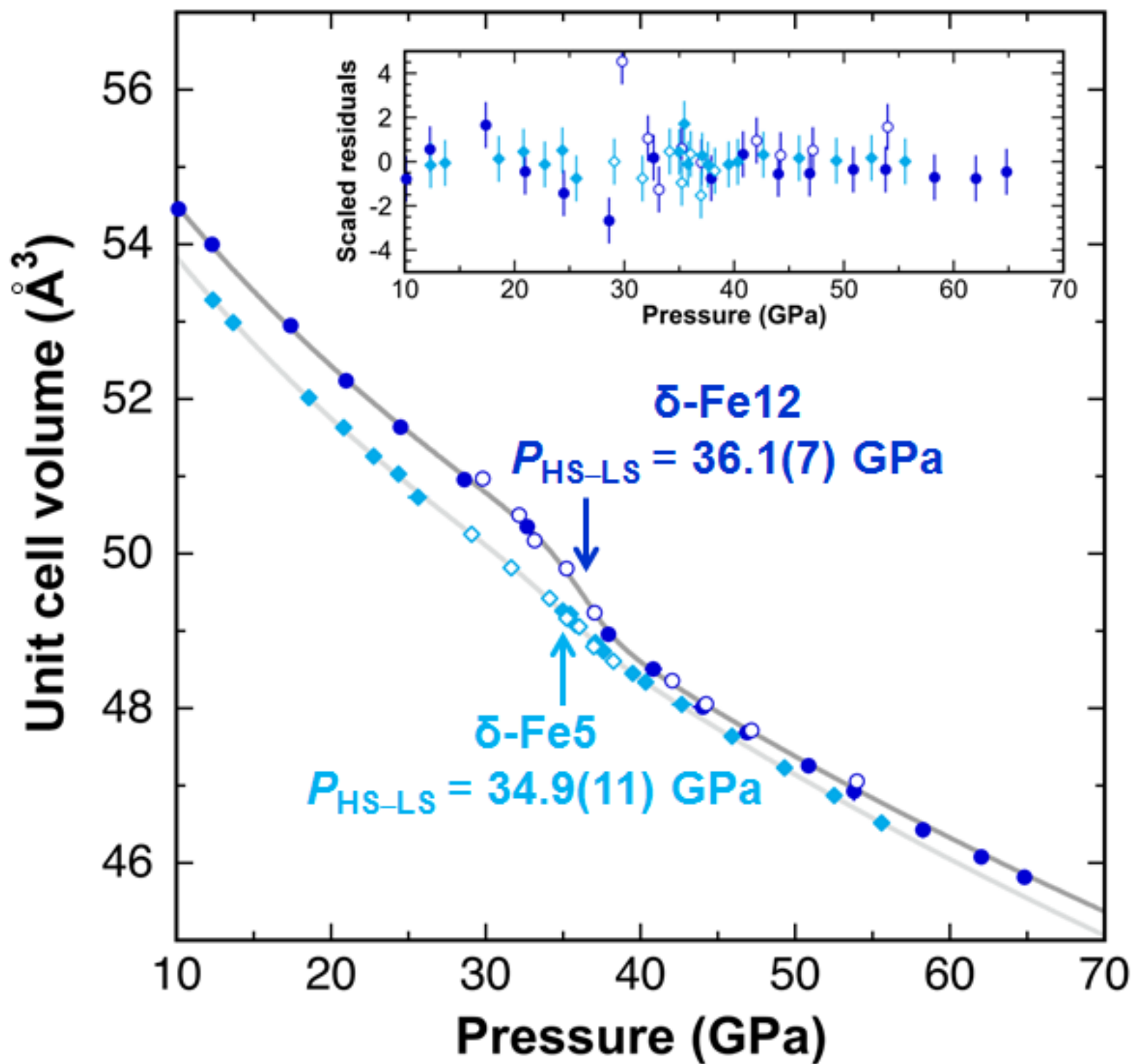


Figure 6

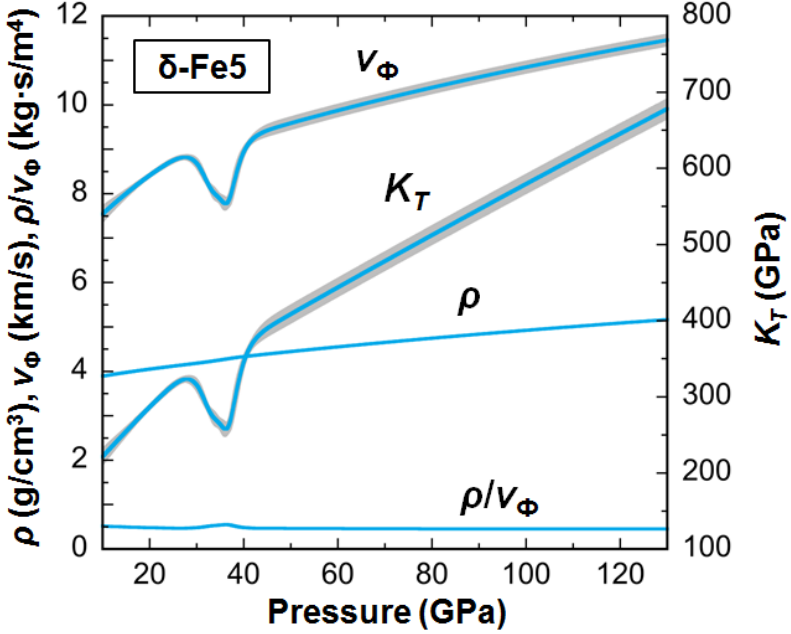
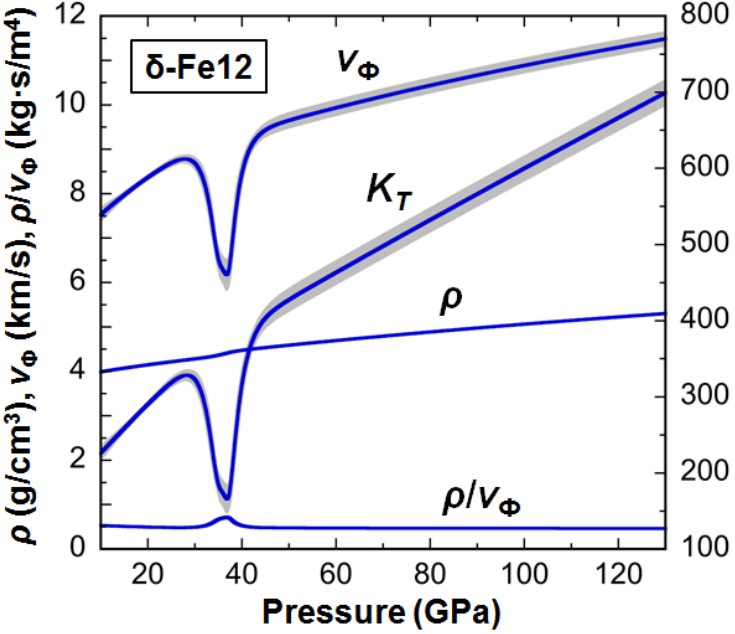
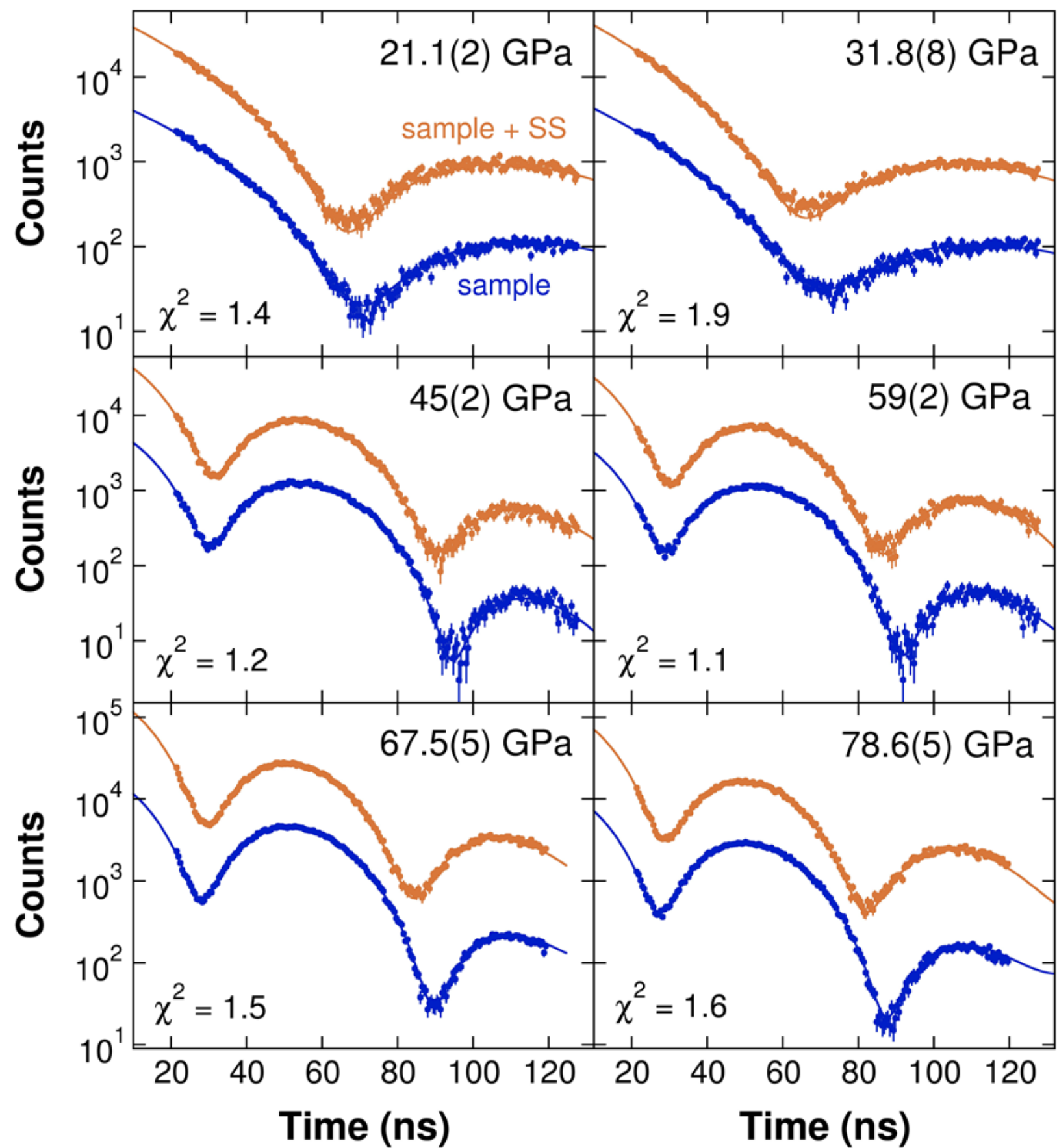
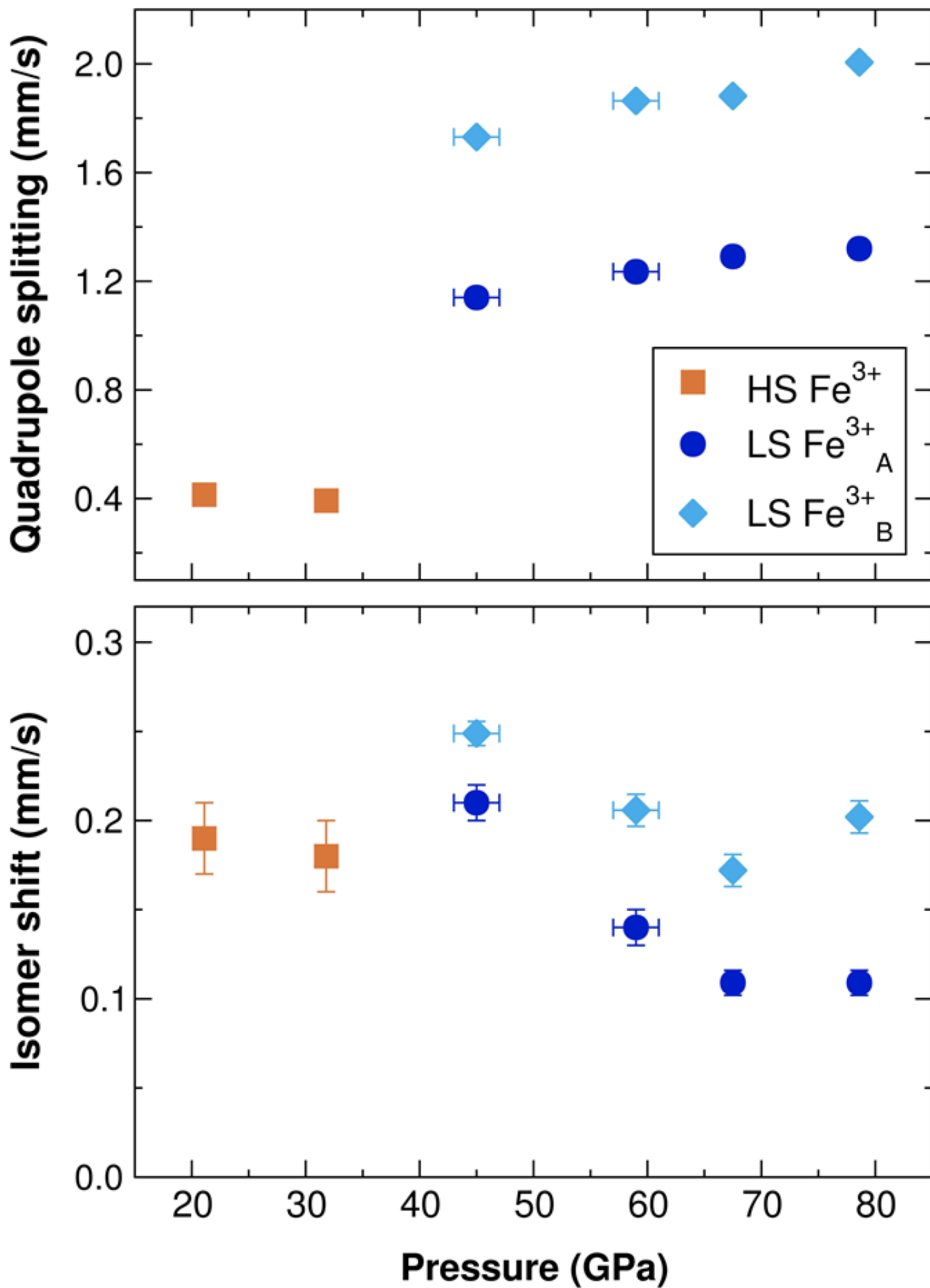


Figure 7



**Figure 8**



**Figure 9**

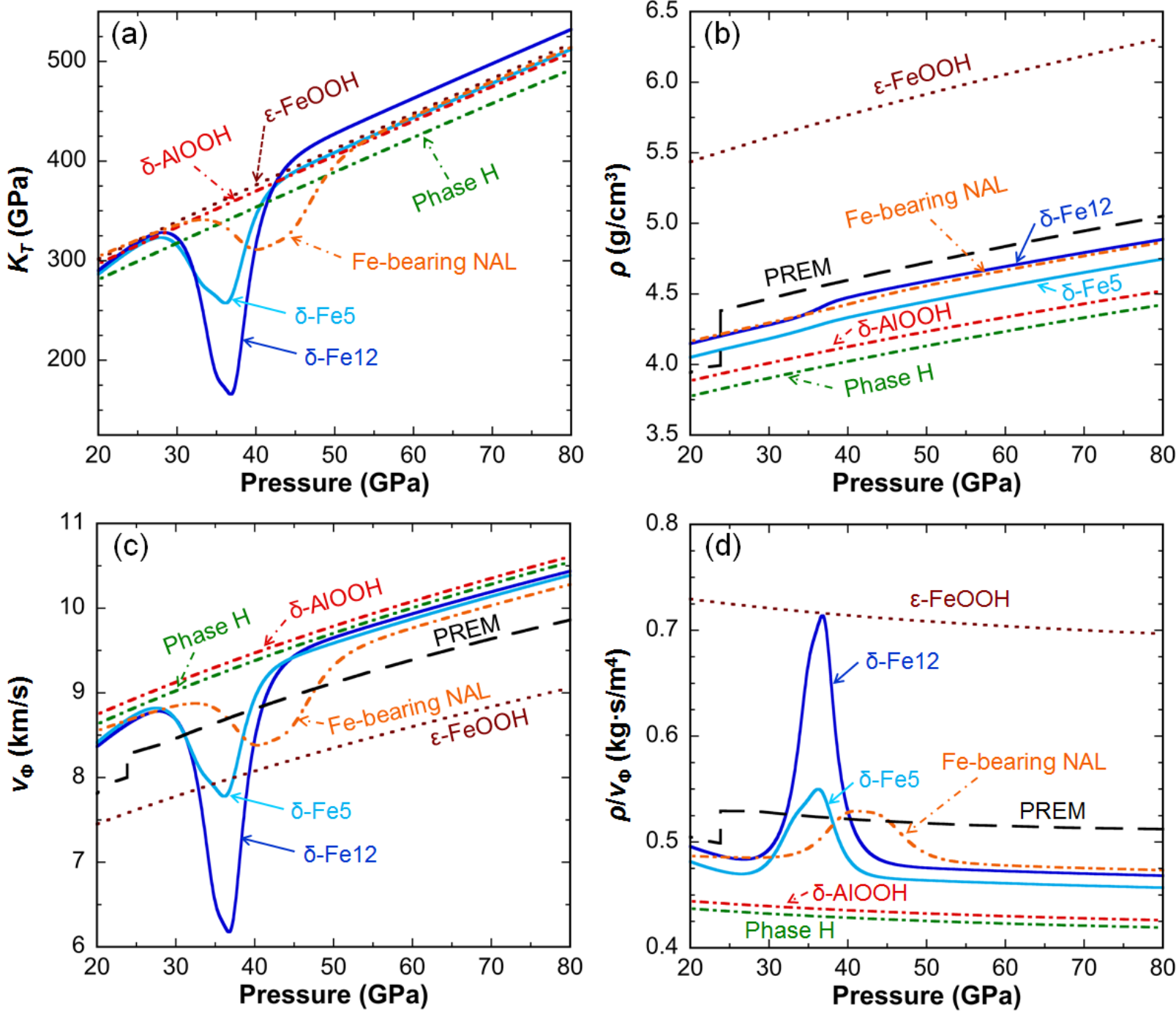




**Table 1.** Lattice constants and unit cell volumes determined for  $\delta$ -Fe12,  $\delta$ -(Al<sub>0.832(5)</sub><sup>57</sup>Fe<sub>0.117(1)</sub>)OOH<sub>1.15(3)</sub> (Fe/(Al+Fe) = 0.123(

$P_W$ (GPa)	$P_{\text{ruby}}$ (GPa)	$a$ (Å)	$b$ (Å)	$c$ (Å)	$V$ (Å <sup>3</sup> )
<i>Compression</i>					
1.07(1)		4.7401(4)	4.2488(8)	2.8522(2)	57.44(3)
2.01(5)	1.62(8)	4.7301(3)	4.2376(5)	2.8486(1)	57.10(2)
4.65(3)	4.18(11)	4.7048(4)	4.2062(6)	2.8379(2)	56.16(2)
6.00(2)	5.54(15)	4.6919(3)	4.1920(5)	2.8321(2)	55.70(2)
7.71(5)		4.6781(4)	4.1725(5)	2.8256(2)	55.15(3)
7.83(2)		4.6762(5)	4.1711(6)	2.8248(2)	55.10(3)
10.13(6)	9.49(25)	4.6591(2)	4.1520(4)	2.8154(1)	54.46(2)
12.29(11)	11.86(1)	4.6456(4)	4.1403(6)	2.8075(2)	54.00(3)
17.38(5)	16.57(33)	4.6148(2)	4.1147(3)	2.7884(1)	52.95(1)
20.96(6)		4.5951(4)	4.0971(7)	2.7753(2)	52.24(3)
24.47(4)	23.76(30)	4.5763(2)	4.0832(3)	2.7637(1)	51.64(1)
28.62(3)	27.79(29)	4.5565(2)	4.0662(4)	2.7503(1)	50.96(2)
32.67(9)	31.73(22)	4.5373(4)	4.0532(8)	2.7379(3)	50.35(3)
37.93(15)		4.4967(5)	4.0170(8)	2.7104(3)	48.96(3)
40.83(49)		4.4840(6)	4.0065(7)	2.7002(3)	48.51(3)
44.03(58)		4.4703(7)	3.9936(9)	2.6901(4)	48.02(4)
46.88(45)		4.4602(9)	3.9852(18)	2.6829(4)	47.69(7)
50.85(33)		4.4455(10)	3.9750(20)	2.6742(5)	47.26(8)
53.80(35)		4.4351(17)	3.9663(25)	2.6678(7)	46.93(11)
58.27(34)		4.4205(15)	3.9536(22)	2.6568(6)	46.43(9)
62.04(33)		4.4094(9)	3.9434(13)	2.6500(3)	46.08(5)
64.83(35)		4.4009(15)	3.9394(18)	2.6427(6)	45.82(8)
<i>Decompression</i>					
53.97(6)		4.4405(11)	3.9684(15)	2.6704(6)	47.06(7)
47.17(7)		4.4607(6)	3.9851(8)	2.6845(4)	47.72(4)
44.23(11)		4.4707(6)	3.9940(7)	2.6913(4)	48.06(4)
42.06(20)		4.4799(5)	4.0018(8)	2.6974(3)	48.36(3)
37.02(26)		4.5046(3)	4.0255(5)	2.7156(2)	49.24(2)
35.22(28)		4.5222(5)	4.0397(7)	2.7267(2)	49.81(3)
33.16(26)		4.5328(6)	4.0492(9)	2.7334(3)	50.17(4)
32.14(10)		4.5444(6)	4.0556(12)	2.7398(4)	50.50(5)
29.79(5)		4.5586(4)	4.0660(7)	2.7498(2)	50.97(3)

$P_W$  and  $P_{\text{ruby}}$  indicate the pressure values determined using the EoS for tungsten (Dorogokupets and Oganov 2006) which are used as the experimental pressure, and the ruby fluorescence method (Dewaele et al. 2008), respectively. Uncertainties are given in parentheses for the last reported significant digit.

2)).

**Table 2.** Lattice constants and unit cell volumes determined for  $\delta$ -Fe5 ( $\delta$ -(Al<sub>0.908(9)</sub><sup>57</sup>Fe<sub>0.045(1)</sub>)OOH<sub>1.14(3)</sub>) (Fe/(Al+Fe) = 0.047(1))

$P_w$ (GPa)	$P_{\text{ruby}}$ (GPa)	$a$ (Å)	$b$ (Å)	$c$ (Å)	$V$ (Å <sup>3</sup> )
<i>Compression</i>					
2.04(4)		4.7105(3)	4.2200(5)	2.8343(2)	56.34(2)
3.44(14)		4.6946(2)	4.2021(3)	2.8279(1)	55.79(1)
5.50(11)		4.6778(2)	4.1816(4)	2.8207(1)	55.17(2)
8.36(11)	7.73(14)	4.6515(3)	4.1490(4)	2.8091(1)	54.21(2)
12.36(18)		4.6244(2)	4.1244(3)	2.7934(1)	53.28(1)
13.67(30)	12.96(6)	4.6163(2)	4.1171(3)	2.7883(1)	52.99(2)
18.57(11)		4.5873(1)	4.0932(1)	2.7702(0)	52.02(1)
20.82(31)		4.5758(2)	4.0838(3)	2.7628(1)	51.63(1)
22.76(17)		4.5647(3)	4.0751(5)	2.7558(2)	51.26(2)
24.35(25)		4.557(2)	4.0698(4)	2.7511(1)	51.03(2)
25.63(56)	25.68(32)	4.5487(2)	4.0615(4)	2.7458(1)	50.73(2)
34.99(22)		4.5044(4)	4.0248(6)	2.7173(2)	49.26(3)
35.46(9)		4.5030(5)	4.0243(8)	2.7161(3)	49.22(3)
35.80(23)		4.4987(4)	4.0207(7)	2.7135(2)	49.08(3)
37.10(10)		4.4919(4)	4.0149(7)	2.7089(2)	48.85(3)
37.62(34)		4.4893(5)	4.0116(7)	2.7065(2)	48.74(3)
39.51(29)		4.4799(6)	4.0048(9)	2.7003(3)	48.45(4)
40.34(29)		4.4767(6)	4.0016(10)	2.6982(3)	48.34(4)
42.68(63)		4.4680(5)	3.9945(6)	2.6925(2)	48.05(3)
45.91(37)		4.4548(8)	3.9844(12)	2.6839(4)	47.64(5)
49.31(38)		4.4423(9)	3.9747(17)	2.6748(4)	47.23(7)
52.52(17)		4.4296(11)	3.9670(16)	2.6673(4)	46.87(7)
55.60(16)		4.4211(9)	3.9555(18)	2.6601(4)	46.52(7)
<i>Decompression</i>					
38.27(41)		4.4863(5)	4.0095(6)	2.7025(3)	48.61(3)
36.98(14)		4.4910(7)	4.0150(8)	2.7061(4)	48.80(4)
36.06(15)		4.4994(5)	4.0203(8)	2.7120(6)	49.06(4)
35.23(13)		4.5028(4)	4.0229(7)	2.7140(3)	49.16(3)
34.13(12)		4.5117(6)	4.0293(10)	2.7187(4)	49.42(4)
31.65(7)		4.5228(4)	4.0398(6)	2.7266(2)	49.82(3)
29.08(23)		4.5339(2)	4.0510(3)	2.7361(1)	50.25(2)
0.0001		4.7266(7)	4.2389(10)	2.8401(3)	56.90(5)

$P_w$  and  $P_{\text{ruby}}$  indicate the pressure values determined using the EoS for tungsten (Dorogokupets and Oganov 2006) which are used as the experimental pressure, and the ruby fluorescence method (Dewaele et al. 2008), respectively. Uncertainties are given in parentheses for the last reported significant digit.

0)).

**Table 3.** EoS Parameters of  $\delta$ -(Al,Fe)OOH phases.

Phase	$V_0$ ( $\text{\AA}^3$ )	$K_0$ (GPa)	$K'$ (GPa)	EoS	$P$ range
<u>This study</u>					
$\delta$ -(Al <sub>0.832(5)</sub> <sup>57</sup> Fe <sub>0.117(1)</sub> )OOH <sub>1.15(3)</sub>	57.85(2)	147(1)	4 (fixed)	2nd BM	1.0–10.1 GPa
$\delta$ -(Al <sub>0.832(5)</sub> <sup>57</sup> Fe <sub>0.117(1)</sub> )OOH <sub>1.15(3)</sub>	57.5(3)	155(22)	8(2)	Spin crossover EoS	10.1–64.8 GPa
$\delta$ -(Al <sub>0.832(5)</sub> <sup>57</sup> Fe <sub>0.117(1)</sub> )OOH <sub>1.15(3)</sub>	55.2(4)	241(14)	4 (fixed)	Spin crossover EoS	
$\delta$ -(Al <sub>0.908(9)</sub> <sup>57</sup> Fe <sub>0.045(1)</sub> )OOH <sub>1.14(3)</sub>	57.03(7)	152(7)	4 (fixed)	2nd BM	0–8.4 GPa
$\delta$ -(Al <sub>0.908(9)</sub> <sup>57</sup> Fe <sub>0.045(1)</sub> )OOH <sub>1.14(3)</sub>	56.9(4)	149(25)	8(2)	Spin crossover EoS	12.4–55.6 GPa
$\delta$ -(Al <sub>0.908(9)</sub> <sup>57</sup> Fe <sub>0.045(1)</sub> )OOH <sub>1.14(3)</sub>	55.4(3)	223(11)	4 (fixed)	Spin crossover EoS	
<u>Previous study</u>					
$\delta$ -AlOOH	56.408(9)	152(2)	4 (fixed)	2nd BM	0–10 GPa
$\delta$ -AlOOH	55.47(8)	219(3)	4 (fixed)	2nd BM	10–63.5 GPa
$\delta$ -AlOOH	56.408(9)	191(1)	4 (fixed)	2nd BM	0–63.5 GPa
$\delta$ -AlOOH	56.408(9)	162(3)	5.9(2)	3rd BM	0–63.5 GPa
$\delta$ -AlOOH	56.54(9)	252(3)	4 (fixed)	3rd BM	0–22.5 GPa
$\delta$ -AlOOH	56.35(2)	124(2)	13.5(7)	3rd BM	0–17.1 GPa
$\delta$ -AlOOH <sup>a</sup>	167	167	5.0	Vinet	0–28 GPa
$\delta$ -AlOOH <sup>b</sup>	57.57	205	4.3	Vinet	0–150 GPa
$\epsilon$ -FeOOH <sup>c</sup>	66.3(5)	158(5)	4 (fixed)	2nd BM	0–21 GPa
$\epsilon$ -FeOOH	66.20(3)	126(3)	10(1)	3rd BM	0–8.6 GPa
$\epsilon$ -FeOOH	66.278(6)	135(3)	6.1(9)	3rd BM	0–11.1 GPa
$\epsilon$ -FeOOH <sup>d</sup>	58.62(2)	223(2)	4.07(3)	3rd BM	30–140 GPa

Uncertainties are given in parentheses for the last reported significant digit.

HS, high-spin state; LS, low-spin state

a, Theory,  $P2_1nm$  structure.

b, Theory,  $Pnmm$  (HC) structure.

c, Experimental data were obtained at 473–673 K.

d, Theory,  $Pnmm$  (HC) structure and LS state.

---

---

Details

---

$\delta$ -Fe12 (Fe/(Al+Fe) = 0.123(2)),  $P2_1nm$ , HS

$\delta$ -Fe12 (Fe/(Al+Fe) = 0.123(2)),  $Pnmm$ , HS

$\delta$ -Fe12 (Fe/(Al+Fe) = 0.123(2)),  $Pnmm$ , LS

$\delta$ -Fe5 (Fe/(Al+Fe) = 0.047(10)),  $P2_1nm$ , HS

$\delta$ -Fe5 (Fe/(Al+Fe) = 0.047(10)),  $Pnmm$ , HS

$\delta$ -Fe5 (Fe/(Al+Fe) = 0.047(10)),  $Pnmm$ , LS

References

Sano-Furukawa et al. (2009)

Sano-Furukawa et al. (2009)

Sano-Furukawa et al. (2009)

Sano-Furukawa et al. (2009)

Vanpeteghem et al. (2002)

Suzuki (2009)

Tsuchiya and Tsuchiya (2009)

Tsuchiya and Tsuchiya (2009)

Gleason et al. (2008)

Suzuki (2010)

Suzuki (2016)

Thompson et al. (2017)

---

**Table 4.** Hyperfine parameters for  $\delta$ -Fe13 and the corresponding reduced  $\chi^2$  produced from fitting the spectra of the sample w reference foil simultaneously. Uncertainties are given in parentheses for the last reported significant digit. Isomer shifts are rel Fe13,  $Fe^{3+}_B/(Fe^{3+}_A + Fe^{3+}_B)$  was found to be 1/3 through Monte-Carlo searches and did not change with pressure, and so was f correlations. See text for more details.

<u>HS</u>						
Pressure (GPa)	QS (mm/s)	IS (mm/s)	FWHM (mm/s)	Thickness ( $\mu$ m)	reduced $\chi^2$	
21.1(2)	0.414(7)	0.19(2)	0.12(1)	23.8(5)	1.36(6)	
31.8(8)	0.392(3)	0.18(2)	0.01(5)	26.4(2)	1.88(7)	

<u>LS</u>						
Pressure (GPa)	QS <sub>A</sub> (mm/s)	IS <sub>A</sub> (mm/s)	FWHM <sub>A</sub> (mm/s)	QS <sub>B</sub> (mm/s)	IS <sub>B</sub> (mm/s)	FWHM <sub>B</sub> (mm/s)
45(2)	1.140(4)	0.209(7)	0.260(4)	1.73(1)	0.249(7)	0.16(1)
59(2)	1.235(6)	0.135(8)	0.221(5)	1.864(7)	0.206(9)	0.22(1)
67.5(5)	1.291(6)	0.107(6)	0.215(4)	1.88(1)	0.172(9)	0.28(2)
78.5(5)	1.320(6)	0.109(7)	0.227(4)	2.006(9)	0.202(9)	0.28(2)

with and without the stainless steel  
relative to  $\alpha$ -Fe metal. In low-spin  $\delta$ -  
fixed to reduce parameter

Thickness ( $\mu\text{m}$ )	reduced $\chi^2$
19.8(5)	1.23(5)
18.0(4)	1.12(5)
16.9(2)	1.50(6)
16.1(2)	1.61(6)



**Table 5.** Euler angles  $\alpha$  and  $\beta$  for the electric field gradient orientation of high-spin (HS) and low-spin (LS) ferric iron sites

	$\alpha$	$\beta$
HS Fe <sup>3+</sup>	0°	0°
LS Fe <sup>3+</sup> <sub>A</sub>	296°	261°
LS Fe <sup>3+</sup> <sub>B</sub>	22°	253°

in  $\delta$ -Fe13.